

1 **Membrane constriction and thinning by sequential** 2 **ESCRT-III polymerization**

3
4 Henry C. Nguyen¹, Nathaniel Talledge^{1,2,†}, John McCullough², Abhimanyu Sharma³, Frank R.
5 Moss III¹, Janet H. Iwasa², Michael D. Vershinin^{3,4,5}, Wesley I. Sundquist^{2,*}, Adam Frost^{1,2,6,*}

6
7 ¹Department of Biochemistry & Biophysics, University of California, San Francisco, San Francisco, CA

8 ²Department of Biochemistry, University of Utah, Salt Lake City, UT

9 ³Department of Physics & Astronomy, University of Utah, Salt Lake City, UT

10 ⁴Department of Biology, University of Utah, Salt Lake City, UT

11 ⁵Center for Cell and Genome Science, University of Utah, Salt Lake City, UT

12 ⁶Chan Zuckerberg Biohub, San Francisco, CA

13 [†]Present Address: Institute for Molecular Virology, University of Minnesota-Twin Cities, Minneapolis, MN

14 *For correspondence: wes@biochem.utah.edu and adam.frost@ucsf.edu

15

16 **Abstract**

17 The Endosomal Sorting Complexes Required for Transport (ESCRTs) mediate diverse
18 membrane remodeling events. These activities typically require ESCRT-III proteins to stabilize
19 negatively-curved membranes, although recent work has indicated that certain ESCRT-IIIs also
20 participate in positive-curvature membrane shaping reactions. ESCRT-IIIs polymerize into
21 membrane-binding filaments, but the structural basis for negative versus positive membrane
22 curvature shaping by these proteins remains poorly understood. To learn how ESCRT-IIIs shape
23 membranes, we determined structures of human membrane-bound CHMP1B-only, membrane-
24 bound CHMP1B+IST1, and IST1-only filaments by electron cryomicroscopy. Our structures show
25 how CHMP1B first polymerizes into a single-stranded helical filament, shaping membranes into
26 moderate-curvature tubules. Subsequently, IST1 assembles a second strand upon the CHMP1B
27 filament, further constricting the membrane tube and reducing its diameter nearly to the fission
28 point. Each step of constriction, moreover, thins the underlying bilayer and lowers the barrier to
29 membrane fission. Together, our structures reveal how a two-component, sequential
30 polymerization mechanism drives membrane tubulation, tube constriction, and bilayer thinning.

31

32 Introduction

33 The Endosomal Sorting Complexes Required for Transport (ESCRT) belong to an
34 evolutionarily conserved pathway that mediates membrane remodeling and fission events
35 throughout the cell. The ESCRT machinery comprises staged complexes, including the early-
36 acting ALIX, ESCRT-I, and -II factors and the late-acting ESCRT-III factors and VPS4 family of
37 AAA+ ATPases. Early-acting factors bind to site-specific adaptors and then recruit the late-acting
38 factors that constrict and sever the target membrane. First discovered for their role in the formation
39 of multivesicular bodies (MVBs), ESCRT proteins serve essential functions in an expanding range
40 of cellular processes. Beyond MVBs, these processes include: cytokinetic abscission; egress of
41 enveloped viruses; sealing holes in nuclear, endosomal, and plasma membranes (1-9); and in
42 peroxisome biogenesis and function (10, 11). ESCRT-III proteins primarily shape negatively-
43 curved membranes, such as the necks of budding viruses or intraluminal vesicles, but we and
44 others have shown that some ESCRT-III proteins can also stabilize positively-curved membranes
45 (12-15). Despite their importance to the cell, the mechanisms that govern how ESCRT-III proteins
46 assemble and catalyze membrane remodeling reactions—of either positive or negative
47 membrane curvature—remain unclear.

48 Humans have 12 different ESCRT-III proteins that share a conserved secondary structure
49 core, including helices α 1- α 5. X-ray crystal structures of IST1 and CHMP3 revealed how these
50 helices fold into a compact conformation referred to as a “closed” state (16-18). Other ESCRT-
51 III proteins can adopt more elongated “open” states that can also polymerize (16, 19-21).
52 Structures of such open, elongated and assembled states are available for human CHMP1B (14),
53 *S. cerevisiae* Snf7 (22), and *D. melanogaster* Shrub (23). ESCRT-III polymerization may be
54 regulated by reversible switching between closed and open conformations. Such conformational
55 transitions could be regulated by protein-protein interactions with nucleating factors like the early-
56 acting ALIX or ESCRT-II factors, by membrane curvature (24), or by post-translation

57 modifications, such as ubiquitination, which can sterically hinder membrane-binding or
58 polymerization (25).

59 We previously reported a ~ 4 Å resolution electron cryomicroscopy (cryoEM) structure of
60 a helical filament containing CHMP1B and IST1 (14). This copolymer structure was surprising as
61 it consisted of two distinct strands: an inner strand of CHMP1B in an open conformation and an
62 outer strand of IST1 in a closed conformation. The IST1 strand was tightly associated with the
63 CHMP1B strand with 1:1 stoichiometry. The luminal cavity of the copolymer was strongly
64 positively charged and capable of shaping negatively charged membranes into positive-curvature
65 membrane tubes in vitro and in vivo. Consistently, studies in living cells have shown that CHMP1B
66 and IST1 co-localize with the VPS4 family member SPASTIN along the positive curvature
67 surfaces of endosomal tubules and contact sites between lipid droplets and peroxisomes (10, 14,
68 15, 26). To better understand these new properties and roles for CHMP1B and IST1, and the still
69 unknown structural mechanism by which any ESCRT-III protein interacts with lipid bilayers, we
70 sought to understand how CHMP1B and IST1 work together to bind and constrict membranes.

71

72 **Results**

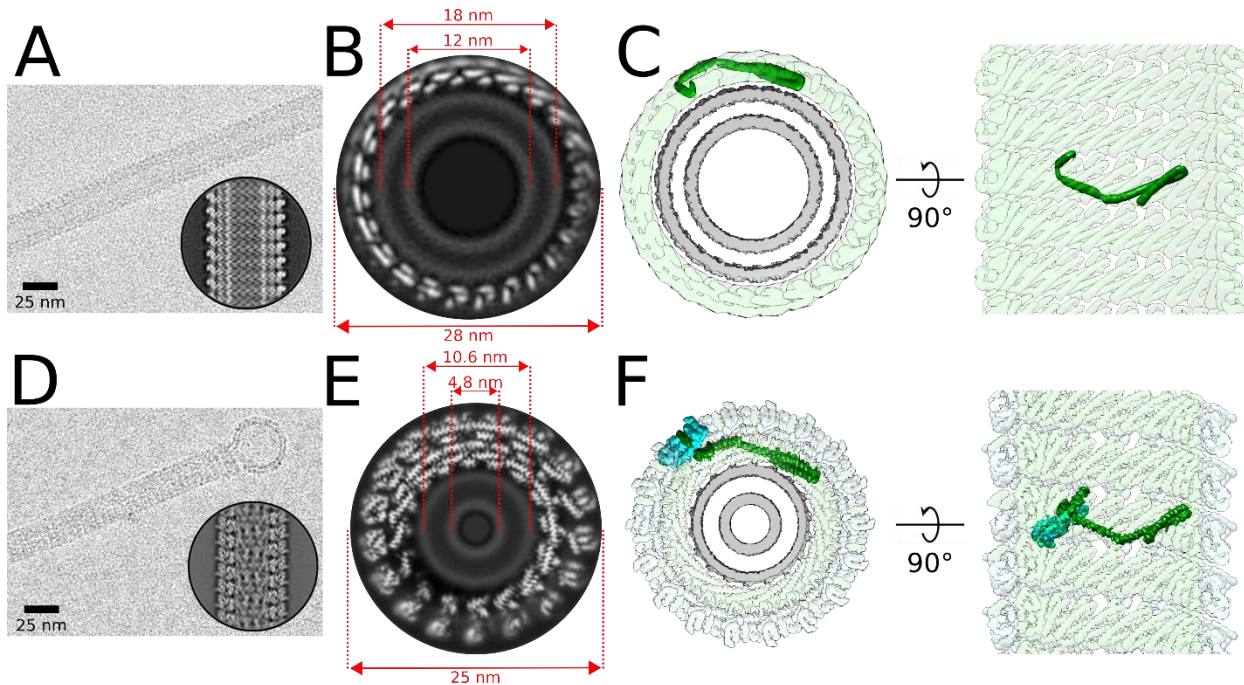
73 *Structure of the membrane-bound CHMP1B filament*

74 To learn how CHMP1B and IST1 remodel positively curved membranes, we sought to
75 capture stable membrane-bound polymers composed of these proteins. We previously showed
76 that incubating liposomes with CHMP1B led to formation of membrane tubules coated with protein
77 filaments (14). To increase the yield and stability of these membrane tubules, we optimized the
78 lipid composition and found that CHMP1B could remodel a variety of different liposome
79 compositions into tubules. Two factors, in particular, enhanced the prevalence and stability of
80 membrane-bound filaments for cryoEM analysis (Figure 1A and 1D): 1) incorporation of
81 polyunsaturated lipids (16:0-22:6 phosphocholine, SDPC) to increase membrane malleability (27,
82 28); and 2) increasing the concentration of negatively charged phospholipids such as PI(3)P

83 (phosphatidylinositol 3-phosphate), PI(3,5)P₂, or PI(4,5)P₂ to complement the highly basic charge
84 of the CHMP1B lumen (14). For our in-depth studies, we settled on liposomes containing 58 mol%
85 SDPC / 18 mol% POPS / 18 mol% cholesterol / 6 mol% PI(3,5)P₂.

86 From this optimized lipid mixture, we first analyzed CHMP1B-only membrane tubes and
87 found that they exhibited a range of diameters (~26-30 nm). This heterogeneity precluded high-
88 resolution studies, but by sorting the tubes based on diameter, we were able to reconstruct a 28
89 nm diameter tube to ~6 Å resolution. This reconstruction unambiguously showed the open-state
90 conformation of CHMP1B and the interconnected network of protomers within the single-
91 stranded, right-handed filament (Figure 1B–1C, Figure 1—figure supplement 1, Tables 1-3). Upon
92 membrane tubulation, the membrane tube diameter, the distance between outer leaflet phosphate
93 headgroups, narrows from >50 nm in the starting, spherical liposomes down to ~18 nm in the
94 CHMP1B-constricted cylindrical state. The inner leaflet headgroups are separated by ~12 nm.
95 Thus, the energy of CHMP1B self-assembly upon the membrane is sufficient to remodel low-
96 curvature membrane spheres into moderate-curvature membrane cylinders.

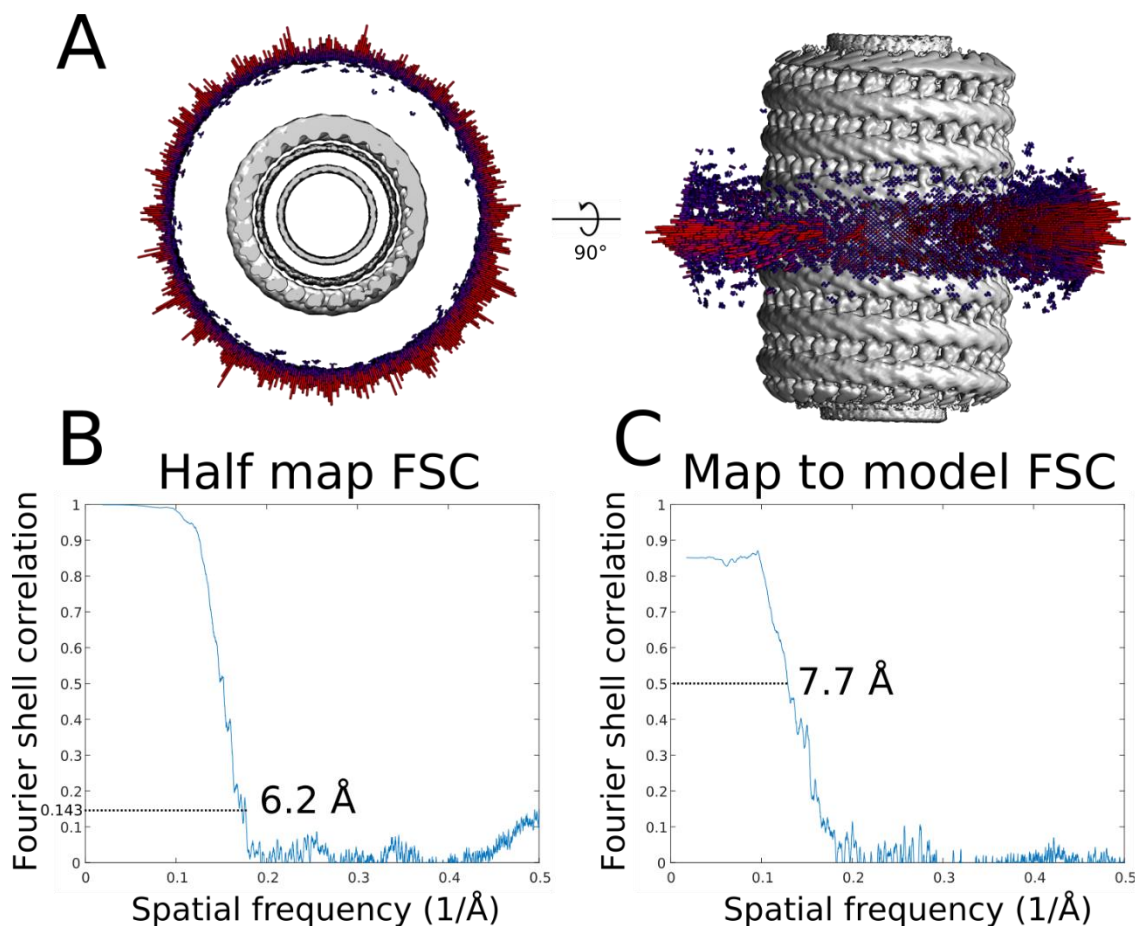
97



98
99
100
101
102
103
104
105
106
107
108
109
110
111
112
113
114
115
116

Figure 1. CHMP1B and IST1 sequentially constrict membrane tubes.

(A) CryoEM micrograph of a membrane-bound CHMP1B tubule. Scale bar: 25 nm. Inset, representative 2D class average. (B) A grey-scale slice looking down the helical axis of the 3D cryoEM reconstruction of the membrane-bound CHMP1B filament. Diameters of the entire tube and the membrane leaflet peak-to-peak distances are annotated. (C) *Left*, surface representation of the same end-on view as in B down the helical axis. CHMP1B (green) coats the exterior of the membrane bilayer (grey). A CHMP1B protomer is highlighted in dark green. *Right*, internal view looking outward from the surface of the membrane. (D) IST1 further constricts the CHMP1B-membrane filament nearly to the hemifission point. CryoEM micrograph of a membrane-bound CHMP1B+IST1 filament with a vesicle protruding from the end. Scale bar: 25 nm. Inset, representative 2D average. (E) A grey-scale slice looking down the helical axis of the 3D cryoEM reconstruction of the membrane-bound, right-handed CHMP1B+IST1 filament. Diameters of the entire tube and membrane leaflet peak-to-peak distances are annotated. (F) *Left*, surface representation of the same end-on view as in E down the helical axis. (*Right*), internal view looking outward from the surface of the membrane. IST1 protomers (cyan) binds to the exterior of CHMP1B (green), leading to constriction of the membrane (grey). IST1 and CHMP1B promoters are highlighted in dark cyan and dark green, respectively.



117
118 **Figure 1—figure supplement 1. CryoEM validation of membrane-bound CHMP1B-only**
119 **filament.**

120 (A) Angular distribution of the membrane-bound CHMP1B filament. (B) Half map Fourier shell
121 correlation (FSC) of the membrane-bound CHMP1B filament. (C) Map to model FSC of the
122 membrane-bound CHMP1B filament.
123

124 *Structures of left- and right-handed membrane-bound CHMP1B+IST1 filaments reveal highly*
125 *constricted bilayers and filament flexibility*

126 We next investigated the effect of sequentially adding IST1 to these filaments by cryoEM.

127 Interestingly, from the same sample we were able to determine two 3D reconstructions of
128 membrane-bound CHMP1B+IST1 filaments, corresponding to approximately equal populations
129 of right- and left-handed helical filaments, to 3.2 Å and to 3.1 Å resolution, respectively (Figure
130 1E–1F, Figure 1—figure supplements 2–3, Tables 1–3). The right-handed CHMP1B+IST1
131 copolymer is a, one-start, double-stranded filament. The outer strand comprises IST1 in the
132 closed conformation, and the inner strand comprises CHMP1B again in the open conformation

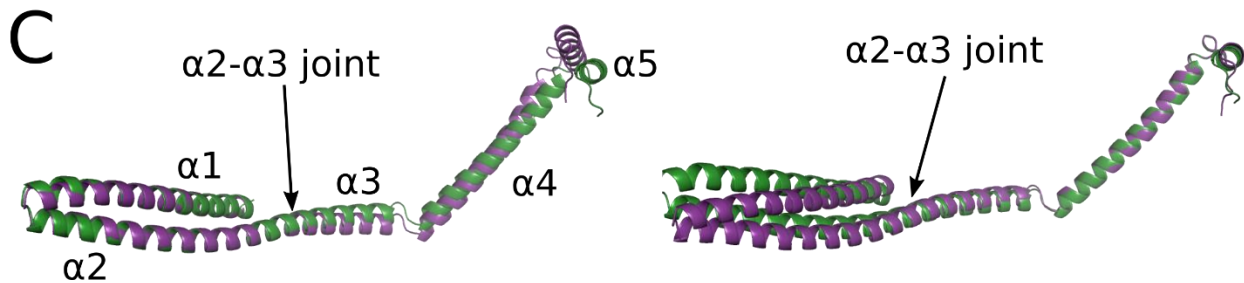
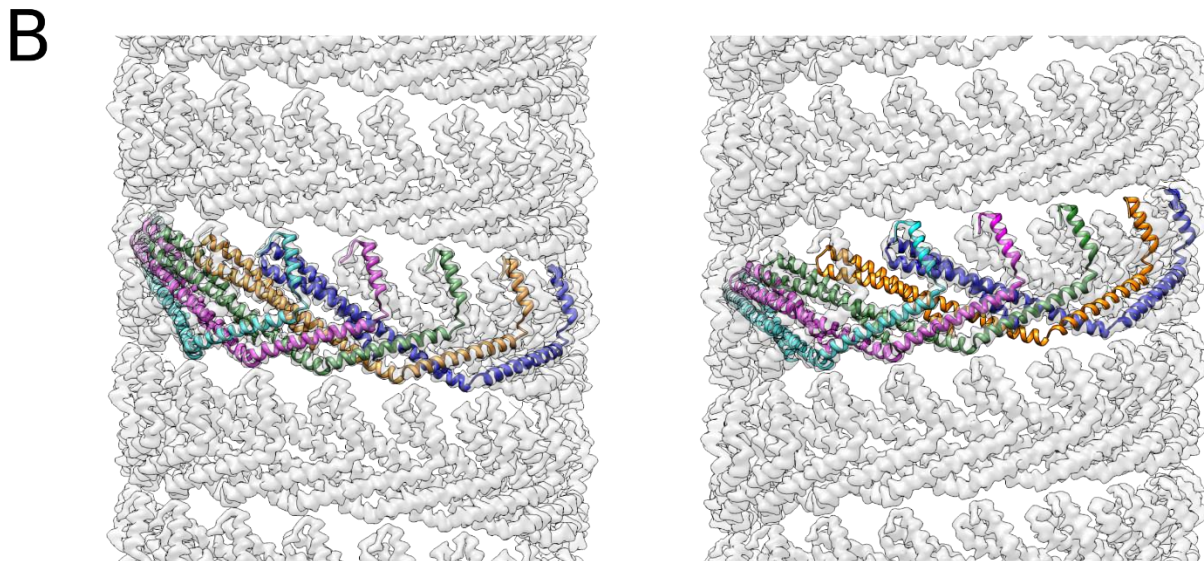
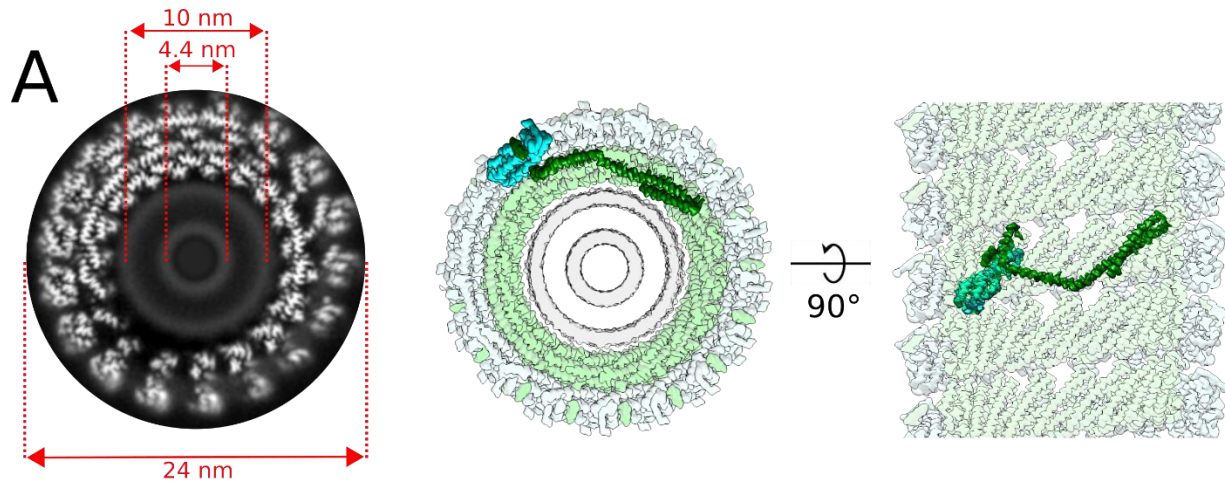
133 (14). The reconstruction also reveals a continuous and highly constricted bilayer within the lumen.
134 The overall outer diameter of the double-stranded filament is 25 nm, slightly narrower than the
135 membrane-bound CHMP1B-only filament. However, due to the presence of two protein strands,
136 the distance between outer leaflet phosphate headgroups is reduced to 10.6 nm, and the distance
137 between inner leaflet headgroups is just 4.8 nm (Figure 1E). Thus, the sequential addition of IST1
138 was sufficient to drive constriction of the CHMP1B strand and the internal membrane, narrowing
139 the luminal inner leaflet diameter from 12 nm down to 4.8 nm.

140 The left-handed helical filament of the membrane-bound CHMP1B+IST1 copolymer also
141 a one-start, double-stranded filament. The left-handed copolymer is slightly more constricted, with
142 an outer diameter of 24 nm and an inner leaflet distance of 4.4 nm (Figure 1—figure supplement
143 2A).

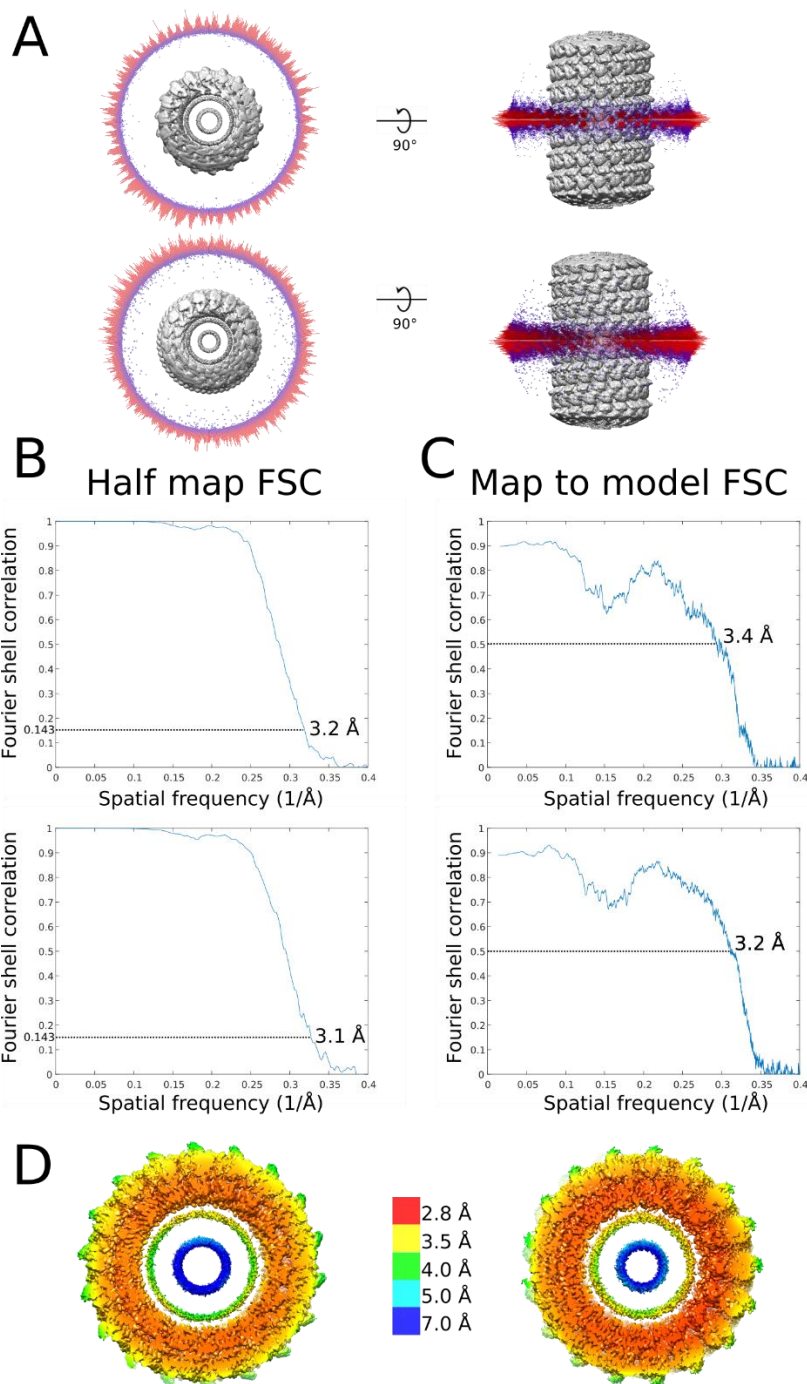
144 Previous work has documented that ESCRT-III filaments (30), like bacterial flagella (31,
145 32), can adopt both left- and right-handed helical structures in vivo. To understand the structural
146 basis of this flexibility, we compared CHMP1B protomer conformations within the left- versus right-
147 handed copolymers (Figure 1—figure supplement 2B–2C). The overall root mean square
148 deviation of the Ca backbone (RMSD) between helices α 1- α 5 of CHMP1B protomers in the two
149 filaments is 1.2 Å. However, the RMSD is smaller when only aligning either the N-terminal helices
150 α 1- α 2 (~0.7 Å) or the C-terminal helices α 4- α 5 (~0.6 Å) (Figure 1—figure supplement 2B–2C).
151 Therefore, switching between a left- or right-handed filament can be achieved simply by a small
152 change in the joint between helices α 2 and α 3 (Figure 1—figure supplement 2B–2C).

153 Sequential assembly of the IST1 strand does not discriminate between the left- and right-
154 handed filaments. The RMSD of single IST1 protomers or between “j” and “j+1” subunits between
155 the two copolymers are only 0.5 Å and 0.6 Å respectively. There are no significant differences in
156 how IST1 assembles around either the left- or right-handed filaments. We envision that as one
157 turn of CHMP1B finishes a revolution, it will either continue polymerizing ‘above’ or ‘below’ the
158 initiating subunit, and this choice will define the helical hand. Thus, it appears that a stochastic

159 flexing between helices $\alpha 2$ - $\alpha 3$ will allow either handedness to propagate. We did not observe left-
160 handed helical polymers in our prior work on the lipid-free or the nucleic-acid templated copolymer
161 structure, perhaps due to the different solution and nucleation conditions that promoted lipid-free
162 polymerization (14, 29). While we did not reconstruct a left-handed membrane-bound CHMP1B-
163 only filament, this likely simply reflects the limited dataset size and diameter variability.



165 **Figure 1—figure supplement 2. CryoEM reconstruction of the membrane-bound**
166 **CHMP1B+IST1 filament at higher curvature and comparison of left- and right-handed**
167 **CHMP1B+IST1 filaments.**
168 (A) CryoEM 3D reconstruction of the membrane-bound left-handed CHMP1B+IST1 filament.
169 End-on view down the helical axis in grey-scale (*left*) or colored (*middle*). *Right*, internal view
170 looking outward from the membrane surface along the helical axis. IST1 protomers (cyan) bind
171 to the exterior of CHMP1B (green), leading to constriction of the membrane (grey). IST1 and
172 CHMP1B promoters are highlighted in dark cyan and green, respectively. Diameters of the
173 entire tube and membrane leaflet peak-to-peak distances are annotated. (B) Electron density
174 maps of CHMP1B from the left-handed (*left*) or right-handed (*right*) membrane-bound
175 CHMP1B+IST1 filaments. Five copies of CHMP1B are shown as ribbons. (C) Superposition of a
176 CHMP1B protomer from the left-handed (purple) and right-handed (green) CHMP1B+IST1
177 filaments aligned to the CHMP1B N-terminal α 1- α 2 helices (*left*) or C-terminal α 4- α 5 helices
178 (*right*).
179



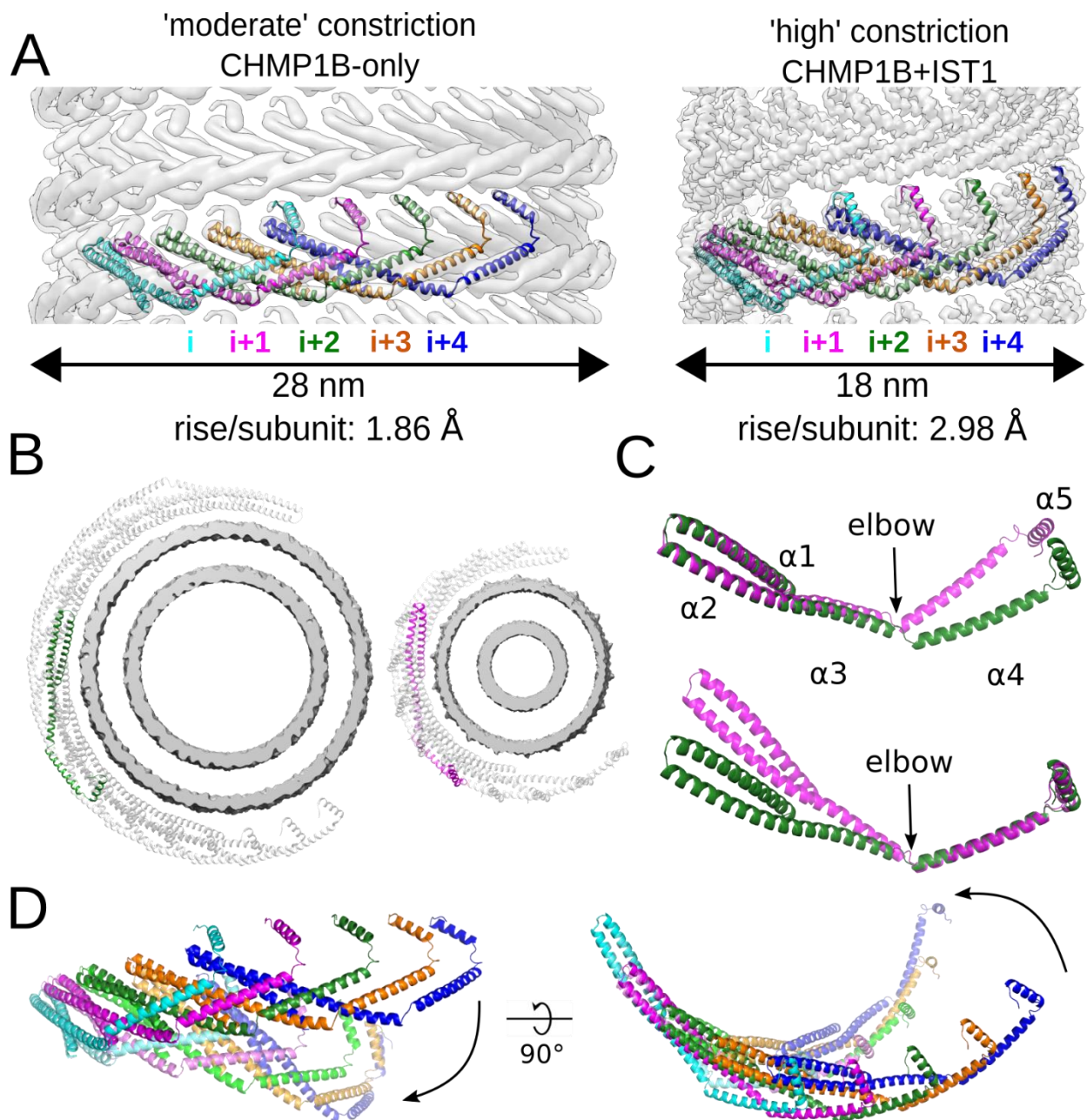
180
181 **Figure 1—figure supplement 3. Local resolution estimates and cryoEM validation of**
182 **membrane-bound CHMP1B+IST1 filaments.**
183 (A) Angular distribution of right-handed (*top*) and left-handed (*bottom*) membrane-bound
184 CHMP1B+IST1 filaments. (B) Half map FSCs of right-handed (*top*) and left-handed (*bottom*)
185 CHMP1B+IST1 filaments. (C) Map to model FSCs right-handed (*top*) and left-handed (*bottom*)
186 CHMP1B+IST1 filaments. (D) Local resolution estimates of right-handed (*left*) and left-handed
187 (*right*) CHMP1B+IST1 filaments.
188

189 *The joint between CHMP1B helices $\alpha 3$ and $\alpha 4$ allows for different curvatures*

190 To understand how CHMP1B polymers adopt different curvatures, we examined how the
191 CHMP1B conformation changes between the “moderate” constriction CHMP1B-only and the
192 “high” constriction CHMP1B+IST1 filaments. In all reconstructions, a single CHMP1B protomer
193 (“i”) interacts with eight other protomers in an interconnected network. Among these, helix $\alpha 5$ of
194 the “i” subunit passes behind three neighboring subunits and binds the closed end of the $\alpha 1$ - $\alpha 2$
195 hairpin of the “i+4” subunit (Figure 2A). Thus, CHMP1B subunits always interweave with the same
196 protomers, regardless of the filament’s overall degree of curvature. There is little contact between
197 neighboring turns of the CHMP1B filament in either state, suggesting that turns can slide past one
198 another during constriction (Figure 2D, Figure 2—movie supplement 1, Figure 2—movie
199 supplement 2).

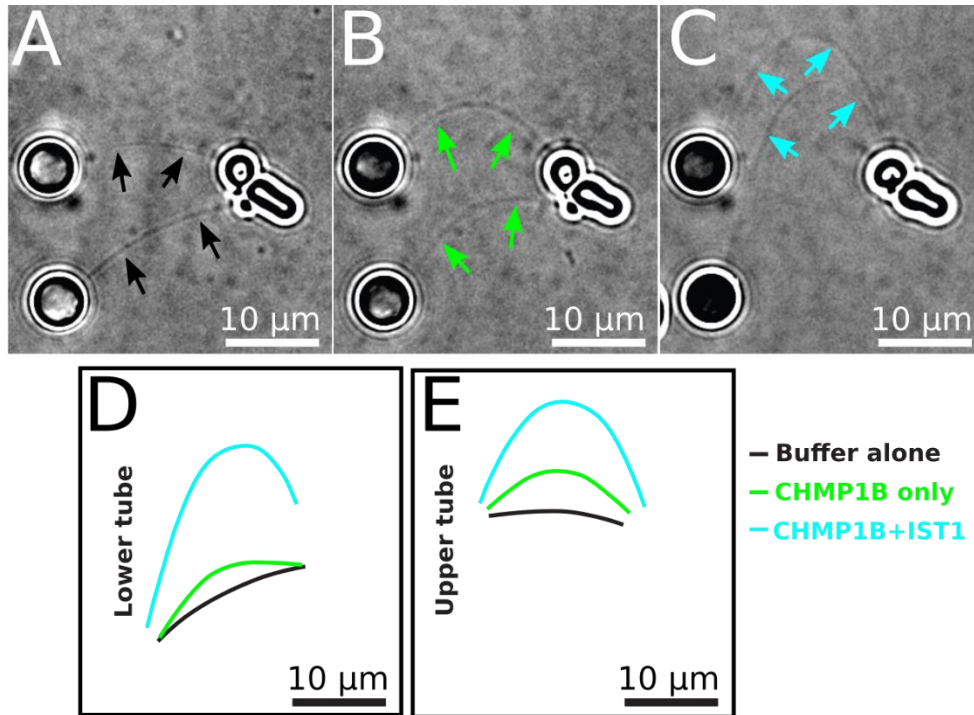
200 We next compared the conformation of a CHMP1B protomer between the CHMP1B-only
201 and the right-handed CHMP1B+IST1 membrane-bound structures (Figure 2C). The RMSD of
202 helices $\alpha 1$ - $\alpha 5$ is 2.4 Å between the two states. However, the RMSD drops to 1.1 Å when
203 comparing only the N-terminal helices $\alpha 1$ - $\alpha 2$. Similarly, comparing just the C-terminal helices $\alpha 4$ -
204 $\alpha 5$ lowers the RMSD to 1.5 Å. While there is again a small change in the angle between helices
205 $\alpha 2$ - $\alpha 3$, the largest conformation difference is at the “elbow” between helices $\alpha 3$ - $\alpha 4$ (Figure 2B-C).
206 This flex in the elbow joint, when propagated across an entire turn of the helical assembly, leads
207 to membrane constriction and also tubule elongation (Figure 2D, Figure 2—movie supplement 1,
208 Figure 2—movie supplement 2). To confirm this tube elongation, we used holographic optical
209 tweezers to hold traptavidin-coated beads and pull membrane tubes from giant unilamellar
210 vesicles (GUVs), and then visualized changes in membrane tube lengths as a function of ESCRT-
211 IIIs. CHMP1B addition elongated the tubes slightly, and subsequent incorporation of IST1
212 produced even longer tubes (Figure 2—figure supplement 1, Figure 2—movie supplement 3). In
213 agreement with our structural studies, tube elongation was dependent on CHMP1B as addition of
214 IST1 alone did not induce membrane elongation (Figure 2—movie supplement 4).

215 Previous work has shown that other ESCRT-IIIs like CHMP2, CHMP3, and CHMP4 also
216 form filaments with a wide range of curvatures (33-35). Owing to the high homology of the ESCRT-
217 III core, we suggest that these proteins also have dynamic elbow joints that will accommodate
218 changes in filament curvature. As noted above, there are minimal contacts between turns of
219 CHMP1B to stabilize inter-turn interactions (Figure 2—movie supplement 2). Indeed, in vivo
220 images of ESCRT-IIIs at different sites of action reveal conical spirals with significant gaps
221 between turns (35-37). Thus, the inherent flexibility of ESCRT-III subunits could allow such loosely
222 packed filaments to form with a range of diameters and helical pitches, and to slide past one
223 another upon constriction.



224
 225
 226 **Figure 2. CHMP1B interlocks in the same arrangement in all structures and flexes at the**
 227 **$\alpha 3$ - $\alpha 4$ elbow to accommodate different curvatures.**
 228 (A) CryoEM density maps of CHMP1B from the membrane-bound CHMP1B (*left*) or right-
 229 handed CHMP1B+IST1 (*right*) filaments. Five interlocked copies of CHMP1B are shown as
 230 ribbons. The C-terminal helix $\alpha 5$ of the i protomer always engages helices $\alpha 1$ - $\alpha 2$ of the $i+4$
 231 protomer. The rise per subunit for each helical filament is denoted. (B) Comparison of arc
 232 curvatures of CHMP1B across the two filaments. Top-down views of half a turn of CHMP1B
 233 subunits are shown for either the CHMP1B (*left*) or CHMP1B+IST1 (*right*) membrane filaments.
 234 The membrane bilayers are shown in grey and the central promoters are shown in green and
 235 magenta for the respective filaments. (C) Superposition of a CHMP1B protomer from the
 236 CHMP1B (green) and CHMP1B+IST1 (magenta) filaments aligned to the CHMP1B N-terminal
 helices $\alpha 1$ - $\alpha 2$ (top) or C-terminal helices $\alpha 4$ - $\alpha 5$ (bottom). The biggest conformational change

237 occurs at the elbow joint. **(D)** Superposition of 5 consecutive subunits (colored from left to right
238 in cyan, magenta, green, orange, and blue) of CHMP1B from the CHMP1B (opaque) and the
239 CHMP1B+IST1 (semi-transparent) filament. The respective first protomers from each are
240 aligned as in (C).



241
242
243
244
245
246
247
248
249

Figure 2—figure supplement 1. Real-time monitoring of CHMP1B and IST1 membrane constriction and elongation.

(A-C) Still images representing deformation of two membrane tubes due to transverse flow of (A) buffer alone, (B) then 0.5 μM CHMP1B, (C) and a final addition of 0.5 μM IST1 is shown. Solid arrows in (A)-(C) highlight tubule locations. (D-E) Contours of lower (D) and upper (E) membrane tubes extracted from panels (A)-(C) showing the extension of the tubes upon addition of CHMP1B and IST1.



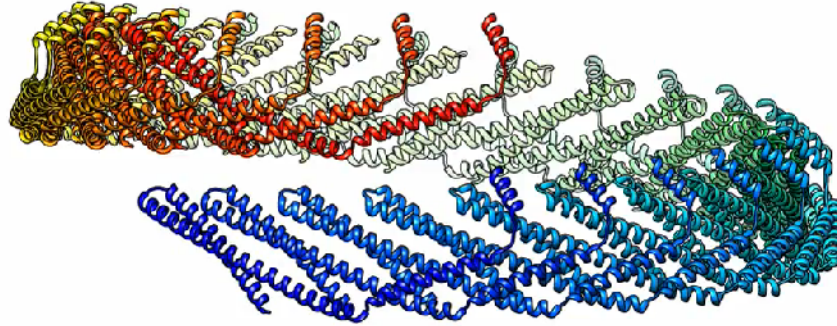
250



251

Figure 2—movie supplement 1. Elbow flexing of one CHMP1B subunit.

252



253

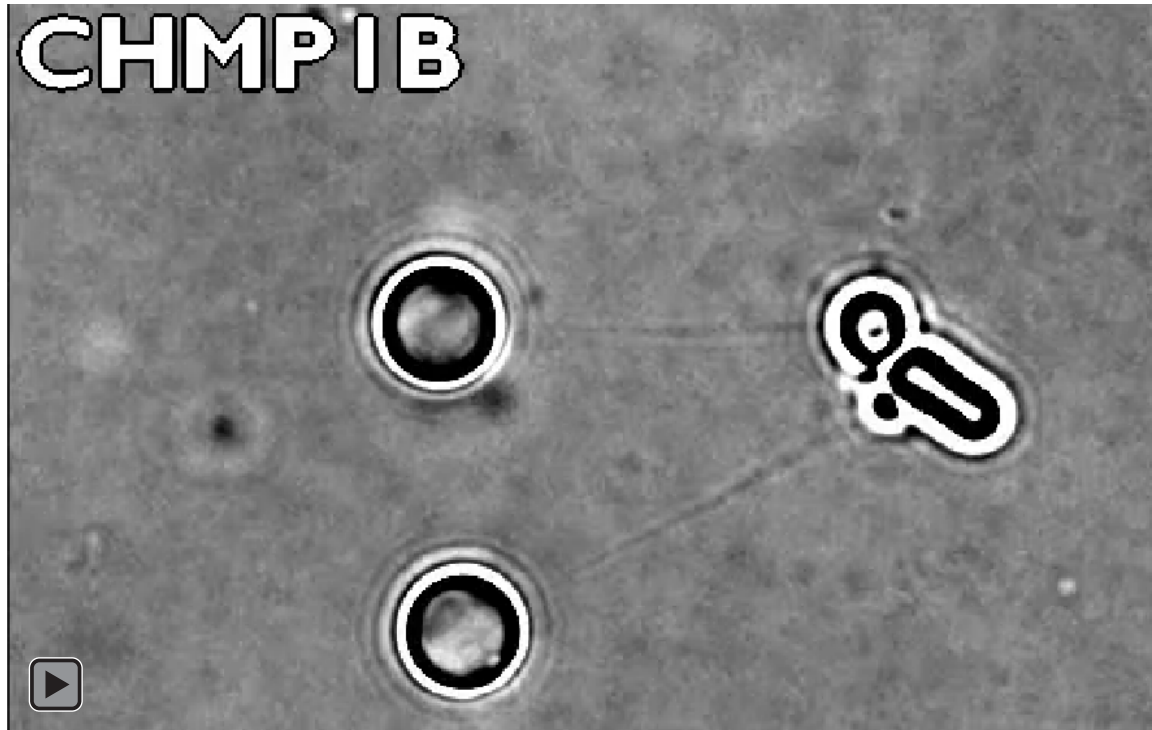


254

255

256

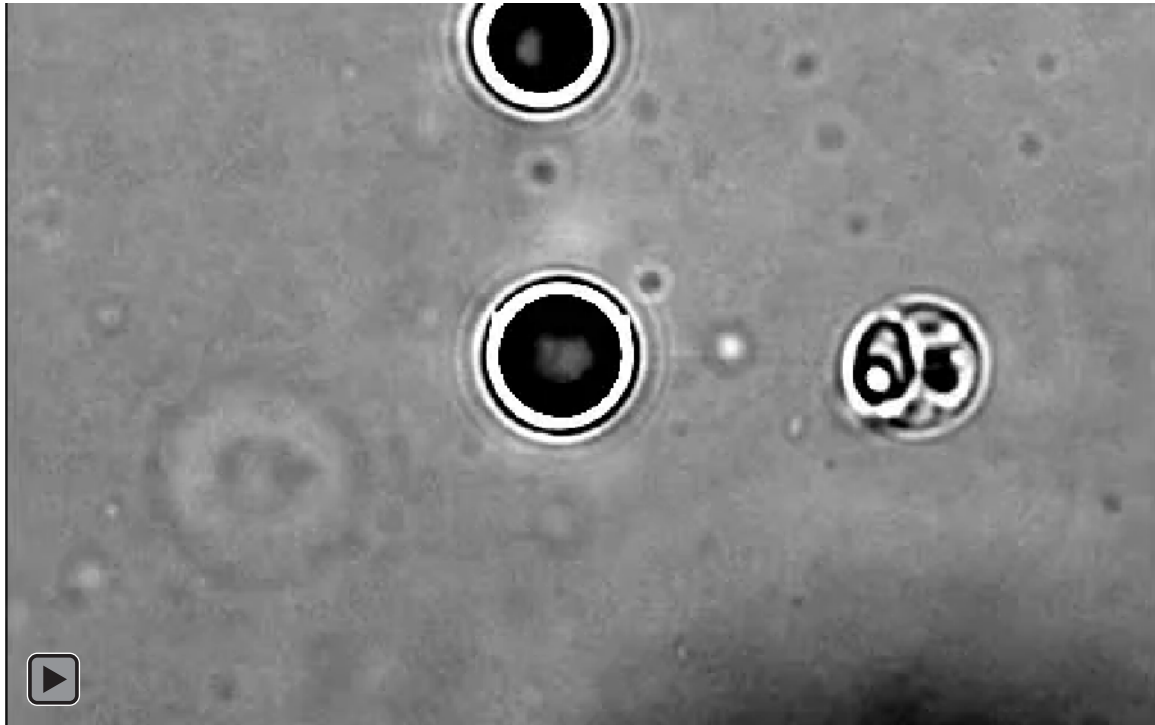
Figure 2—movie supplement 2. Flexing of a full turn of CHMP1B subunits from low to high constriction.



257

258 **Figure 2—movie supplement 3. Real time recording of membrane tube elongation by**
259 **CHMP1B and IST1.**

260



261

262 **Figure 2—movie supplement 4. IST1 alone does not promote membrane tube elongation.**

263

264 *IST1 polymerization drives constriction*

265 To understand how IST1 induces constriction of CHMP1B-membrane filaments, we first
266 docked two IST1 subunits (j and $j+1$) onto sequential CHMP1B protomers (i and $i+1$) of the
267 moderate-curvature CHMP1B-only membrane, based on the CHMP1B-IST1 intersubunit
268 interactions observed in the copolymer filaments (Figure 3A). We then compared how the
269 interactions between IST1 subunits would change between this 'initial IST1 binding' state and
270 those observed in the CHMP1B+IST1 filaments (Figure 3B–3C). The IST1 $j+1$ subunit from the
271 copolymer subunit swings closer (~ 8 Å) to the j subunit when compared to the $j+1$ subunit from
272 the initial IST1 binding state, adding 480 Å² of buried surface area (BSA) (Figure 3—movie
273 supplement 1, Figure 3—movie supplement 2). This swing enables the formation of hydrogen
274 bonds between IST1 residues D77 and R82 on helix $\alpha 3$ of the j subunit with R55 and E57 on helix
275 $\alpha 2$ of the $j+1$ subunit (Figure 3C). In contrast, IST1 subunits make only minimal contacts between
276 adjacent turns (15 Å² of BSA between the j and $j+18$ subunits and no contacts between the $j+1$
277 and $j+18$ subunits). Thus, interactions between the j and $j+1$ subunits along the IST1 strand
278 provide the force that flexes the CHMP1B elbow and consequently constricts and elongates the
279 filament. These sliding, lateral interactions to promote changes in filament architecture have also
280 been observed for the yeast ESCRT-III proteins Snf7 and Vps24 (38).

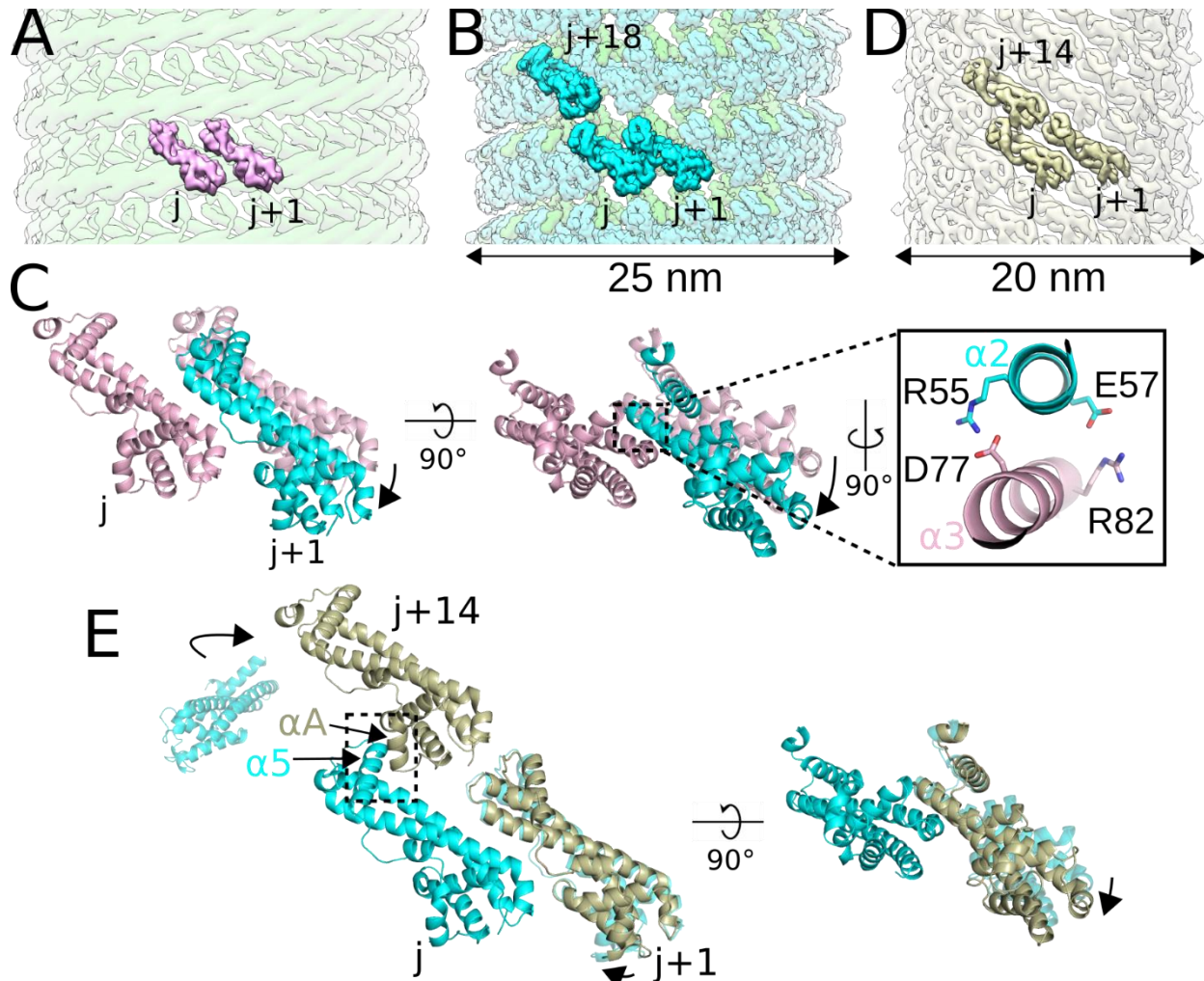
281 IST1 has recently been reported to induce constriction of ESCRT-III assemblies in vitro
282 (39). To understand how IST1 polymerization could drive constriction, we determined a 3D
283 reconstruction of a protein-only IST1 filament (Figure 3D). We previously showed that an N-
284 terminal construct of IST1 (residues 1-189) harboring R16E and K27E mutations (IST1_{NTD}^{R16E/K27E})
285 cannot co-assemble with CHMP1B as the mutations destabilize the CHMP1B-IST1 interface, but
286 can still form tightly-packed homopolymeric helical tubes (14). The IST1-only filaments were
287 heterogeneous in diameter (~ 18 - 28 nm), with the majority of filaments narrower than the
288 CHMP1B+IST1 copolymers (24 - 25 nm). We identified a major subset of IST1_{NTD}^{R16E/K27E} tubes
289 that were ~ 20 nm wide and reconstructed this class to moderate resolution, revealing the

290 secondary structure elements of closed-conformation IST1_{NTD} subunits (Figure 3—figure
291 supplement 1). IST1_{NTD}^{R16E/K27E} forms a single-stranded, right-handed filament (Figure 3D). In the
292 absence of a membrane or CHMP1B, therefore, IST1 alone polymerizes into even narrower
293 helical assembly than either of the copolymers. Interestingly, the reconstruction of these IST1-
294 only filaments revealed that IST1 always adopted the closed conformation, suggesting that IST1
295 may exclusively function in the closed state.

296 To understand how the arrangement of IST1 subunits between IST1-only and
297 CHMP1B+IST1 filaments differ, we compared the interactions of IST1 subunits at the inter-turn
298 interface between the copolymer (j, j+1, and j+18 subunits) and the IST1_{NTD}^{R16E/K27E} (j, j+1, and
299 j+14 subunits) filaments. The RMSD between a protomer from the IST1_{NTD}^{R16E/K27E} filament and
300 an IST1 protomer from the copolymer filament is ~1 Å, with minimal changes in the C α backbone.
301 The j and j+1 contact that defines nearest-neighbor IST1-IST1 interactions is conserved in both
302 structures, but the IST1 j and j+1 subunits swing slightly closer together (~2 Å) in the
303 IST1_{NTD}^{R16E/K27E} filaments (Figure 3E). Propagation of this subtle change actually decreases the
304 BSA between the j and j+1 subunits (from 480 Å² to 340 Å²), but increases inter-turn contacts,
305 which are predominantly made by helix α 5 of the j+1 subunit contacting helix α A of the j+14
306 subunit (220 Å²) and additional packing between the j+1 and j+14 subunits (100 Å²). This results
307 in an overall increase of 165 Å² of BSA at the inter-turn interface for the IST1_{NTD}^{R16E/K27E} filament
308 (Figure 3E). Thus, unlike the constriction seen upon addition of IST1 to the CHMP1B filament,
309 this second constriction step appears to be driven by inter-turn contacts.

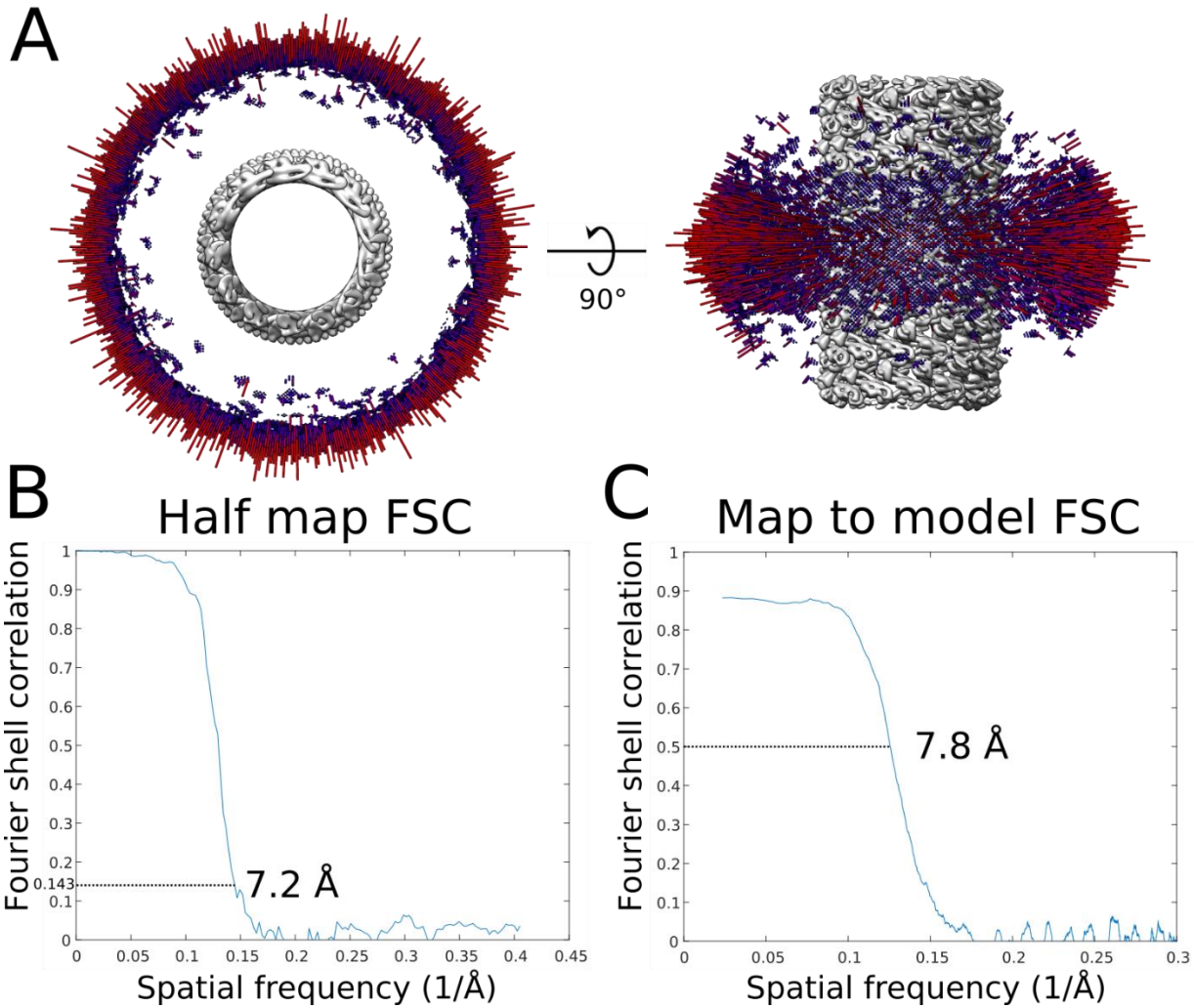
310 We note that the inter-turn interactions involving the j and j+14 subunit in the IST1-only
311 filament are unattainable in the CHMP1B+IST1 filament, as the presence of the CHMP1B helix
312 α 6, the MIT interacting motif (MIM), sterically blocks the IST1 j and j+14 packing (Figure 3—figure
313 supplement 2). Intriguingly, the interaction between IST1 helix α 5 and the CHMP1B MIM supports
314 efficient assembly of the copolymer (29). We speculate that modulation of this interface by the

315 VPS4 family of ATPases could, in principle, regulate the degree of constriction achieved by the
 316 CHMP1B+IST1 filament.



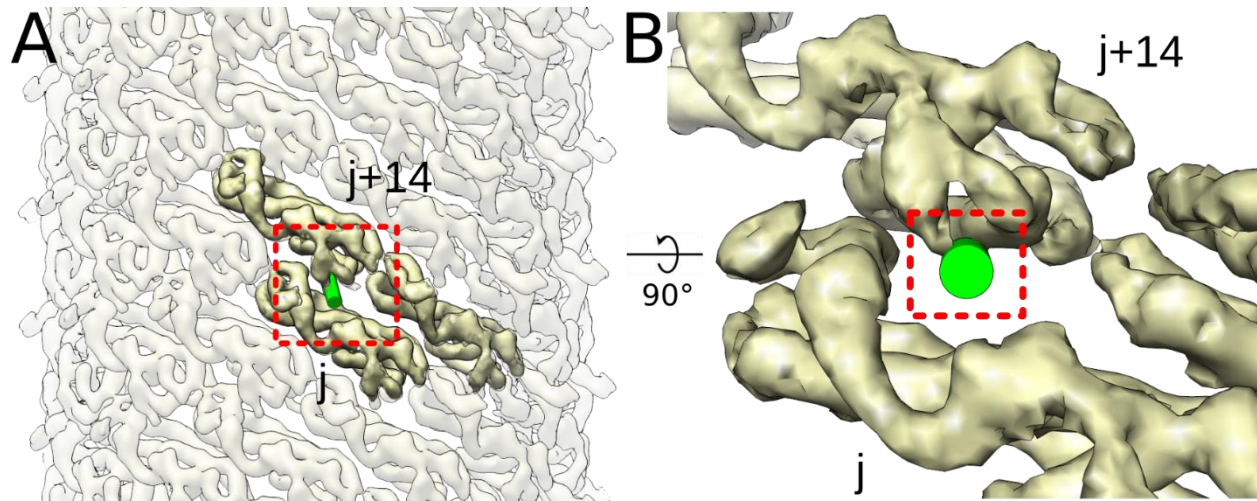
317
 318 **Figure 3. IST1 polymerization drives constriction of the CHMP1B+IST1 filament.**
 319 (A) Model of two IST1 subunits (j, j+1), colored pink, initially binding onto the CHMP1B filament
 320 (green). (B) CryoEM reconstruction of the right-handed CHMP1B+IST1 filament, with CHMP1B
 321 and IST1 in green and cyan, respectively. Three IST1 subunits (j, j+1, j+18) are highlighted.(C)
 322 Superposition of the j and j+1 IST1 subunits from (A) and (B), with the j subunits used for
 323 alignment. (*Inset*), new electrostatic interactions between helix $\alpha 3$ (pink) from the j subunit and
 324 helix $\alpha 2$ (cyan) from the j+1 subunit help stabilize intra-IST1 contacts to drive constriction. (D)
 325 CryoEM 3D reconstruction of the $IST1_{NTD}^{R16E/K27E}$ filament (bronze). Three IST1 subunits (j, j+1,
 326 j+14) are highlighted. (E) Superposition of the j, j+1, and j+14 subunits from the $IST1_{NTD}^{R16E/K27E}$
 327 filament in (D) with IST1 subunits from the CHMP1B+IST1 filament in (B). Protomers were
 328 aligned by the j subunit. The boxed area highlights helix $\alpha 5$ of the j subunit and helix αA from
 329 the j+14 subunit driving inter-turn interactions.

330



331
332
333
334
335

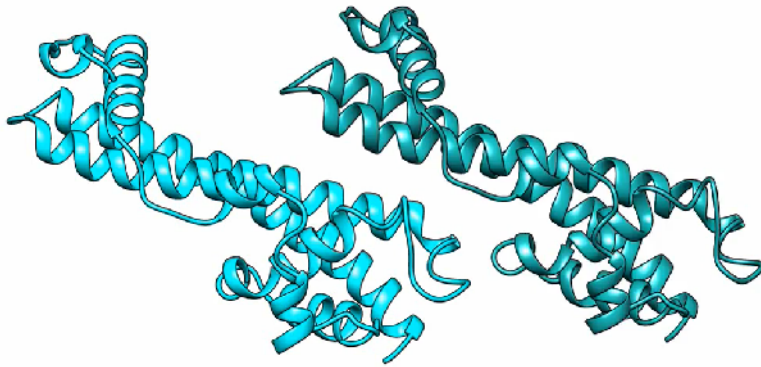
Figure 3—figure supplement 1. CryoEM validation of the IST1_{NTD}^{R16E/K27E} filament.
(A) Angular distribution of the IST1NTDR16E/K27E filament. (B) Half map FSC of the IST1NTDR16E/K27E filament. (C) Map to model FSC of the IST1NTDR16E/K27E filament.



336
337
338
339
340
341
342
343

Figure 3—figure supplement 2. Steric clashing between the CHMP1B MIM and inter-turn IST1 subunits would prevent IST1 from achieving its preferred curvature in the copolymer.

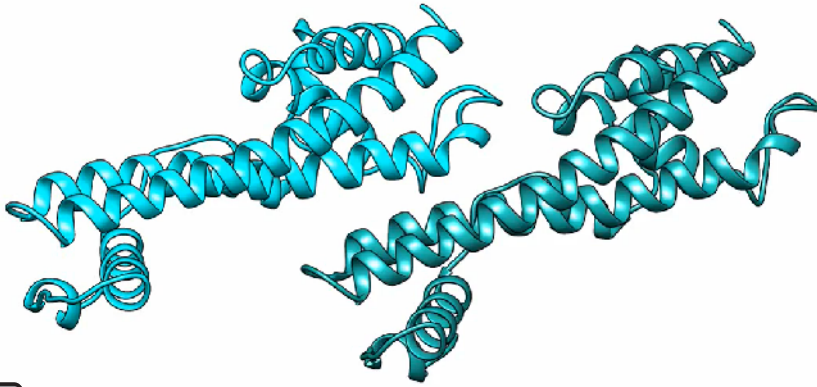
(A) External view of the IST1_{NTD}^{R16E/K27E} filament with one CHMP1B MIM (shown as a green cylinder) docked onto the IST1_{NTD}^{R16E/K27E} j subunit. (B) Zoomed in view of boxed area in (A) highlighting how the CHMP1B MIM clashes with the IST1 j+14 subunit.



344

345 **Figure 3—movie supplement 1. Swinging of two IST1 subunits from initial binding to the**
346 **CHMP1B filament to the constricted state (side view).**

347



348

349 **Figure 3—movie supplement 2. Swinging of two IST1 subunits from initial binding to the**
350 **CHMP1B filament to the constricted state (top-down view).** The membrane would lie at the
351 top of the animation.
352

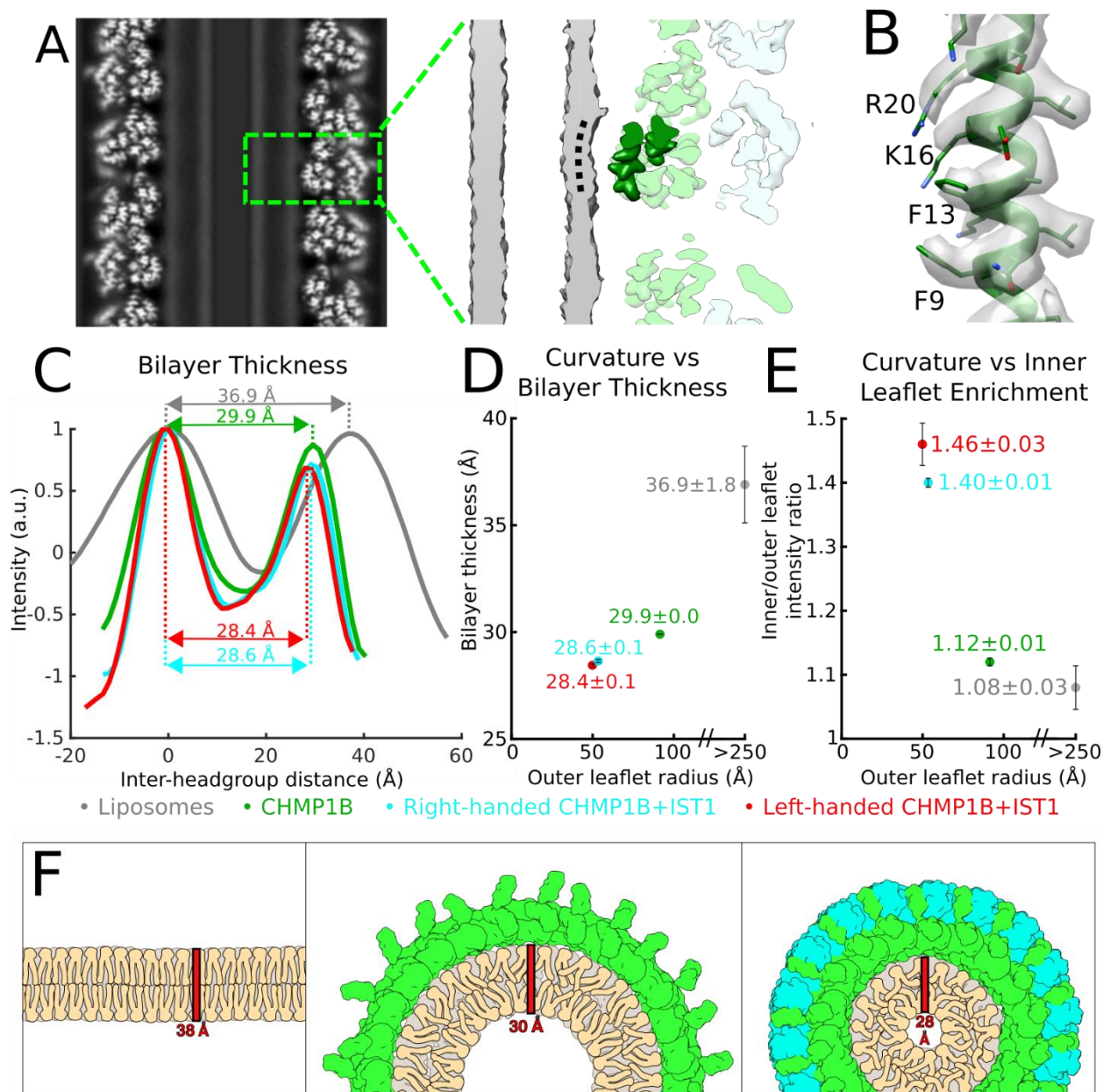
353 *The membrane bilayer thins and the inner leaflet compresses at high curvature*

354 We also examined the consequences to the membrane as a function of increasing
355 curvature stress (Figure 4). In both copolymer reconstructions, helix $\alpha 1$ of CHMP1B faced the
356 membrane, and the surface of the bilayer appeared to be “dimpled” by certain amino acids (Figure
357 4A). Specifically, the conserved CHMP1B residues F9, F13, K16, and R20, which lie on the same
358 face of helix $\alpha 1$, comprise the protein-membrane interface (Figure 4B). No residues appeared to
359 insert deeply into the membrane. Rather, they appear to sit at the hydrated surface of the bilayer.
360 The mixed aromatic and cationic character of the CHMP1B region that most closely approaches
361 the membrane does not suggest any lipid recognition specificity beyond net anionic charge, with
362 the basic residues complementing the negatively charged membrane. It is somewhat surprising
363 that the hydrophobic residues remain fully hydrated at this degree of constriction, but we
364 speculate that they may be poised to insert into the membrane (see below).

365 By measuring the peak-to-peak distances between the outer leaflet and inner leaflet
366 headgroups, we observed a correlation between bilayer thinning and the degree of membrane
367 constriction by CHMP1B and by CHMP1B+IST1. To determine the bilayer thickness of our initial,
368 unconstricted bilayers, we performed small-angle X-ray scattering (SAXS) of our relaxed
369 liposomes. This experiment yielded a thickness estimate of $38.6 \pm 0.6 \text{ \AA}$ (Figure 4—figure
370 supplement 1), consistent with previously published SAXS measurements of membranes
371 composed primarily of SDPC (40). We compared this measurement with bilayer profiles from
372 cryoEM 2D averages of segments of our liposomes, which yielded a thickness of $36.9 \pm 1.8 \text{ \AA}$,
373 which is within the experimental uncertainty of the SAXS measurement (Figure 4C–4D). Upon
374 constriction by CHMP1B alone, the bilayer compressed to $29.9 \pm 0.0 \text{ \AA}$. The sequential addition
375 of IST1 led to further compression of the membrane to $28.6 \pm 0.1 \text{ \AA}$ and $28.4 \pm 0.1 \text{ \AA}$ for the right-
376 handed and left-handed copolymers, respectively (Figure 4C–4D). In addition, the intensity of the
377 inner leaflet increased as a function of constriction, with inner/outer leaflet peak intensities of 1.08
378 ± 0.03 , 1.12 ± 0.01 , 1.40 ± 0.01 , and 1.46 ± 0.03 for the liposomes, moderate-constriction

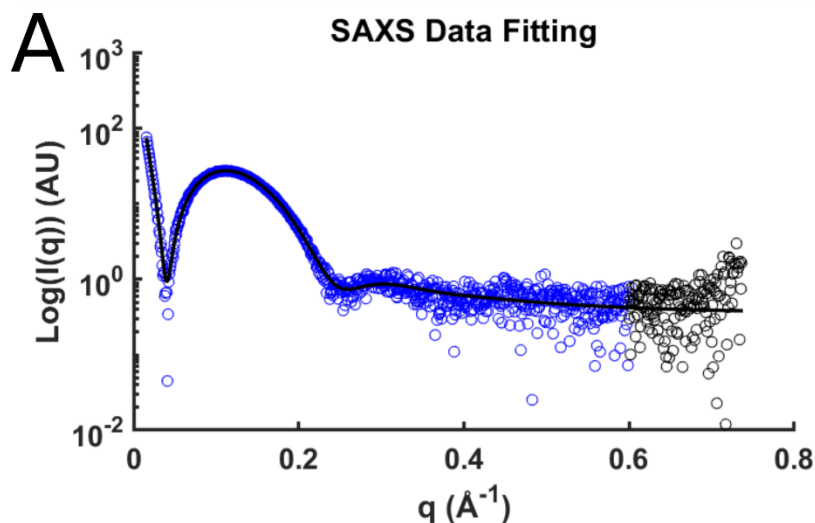
379 CHMP1B filaments, and the high-constriction right-handed and left-handed CHMP1B+IST1
380 filaments, respectively (Figure 4E). Thus, the lipid density in the inner leaflet increases
381 significantly as the membrane tubule constricts towards the fission point.

382 In agreement with physical models of membrane behavior (41, 42), our reconstructions
383 indicate that the bilayer thins as the membrane is constricted (Figure 4C–4D) and that the outer
384 leaflet headgroups separate while the inner leaflet headgroups become more crowded (Figure
385 4E). To accommodate this thinning, the acyl chains from both leaflets likely become more
386 disordered and less extended (Figure 4F). It has also been suggested that curvature stress
387 causes local lipid composition changes that increases the membrane line tension and promote
388 fission (43, 44). We speculate that these changes may lower the activation barrier for fission. With
389 this specific lipid composition, however, the tubes remain stable with only a 4.2 nm gap between
390 the inner leaflet headgroups across the lumen.



391
 392
 393 **Figure 4. The bilayer thins and the inner leaflet crowds under high curvature.**
 394 (A) The outer leaflet buckles under extreme curvature. *Left*, central slice along the helical axis.
 395 *Right*, zoomed view of boxed area in left showing CHMP1B dimpling (black dashed curved line)
 396 in the outer leaflet of the bilayer. A CHMP1B helix $\alpha 1$ sitting at the membrane is highlighted in
 397 dark green. (B) CryoEM density map and model of CHMP1B helix $\alpha 1$ from (A). The residues
 398 involved in membrane binding are labeled. (C) Intensity plots of membrane bilayer thickness for
 399 liposomes only (from 2D class averages, colored in grey), membrane-bound CHMP1B (green),
 400 and right- or left-handed membrane-bound CHMP1B+IST1 filaments (cyan and red
 401 respectively) as determined by cryoEM. The bilayer thickness is labeled for each. Intensities
 402 were normalized to the peak intensity of the inner leaflet. (D) Plot of membrane thickness as a
 403 function of radius of the outer leaflet. The dots are colored as in (left). For (C) and (D), the
 404 liposome values were determined from 2D averages ($n=6$) while the others were determined
 405 from half maps from each 3D reconstruction ($n=2$). (E) The inner membrane density increases
 as a function of curvature. Plot of ratio of inner leaflet to outer leaflet peak intensity as a function

406 of radius of the outer leaflet. Dots are labeled as in (C). (F) Schematic illustration of lipid
407 behavior as the bilayer is remodeled from planar (*left*), to moderate curvature by CHMP1B
408 (*middle*), to high curvature by CHMP1B+IST1 (*right*). The outer leaflet headgroups spread out,
409 while the inner leaflet headgroups crowd and the aliphatic tails become more disordered and
410 therefore less extended.



B

ρ_1	ϵ_1	σ_1	ρ_2	σ_2	ρ_3	ϵ_3
1.23	-18.3	7.4	-1.00	7.6	1.84	20.3
± 0.02	± 0.4	± 0.1	± 0.02	± 0.1	± 0.04	± 0.4

σ_3	l_0 [$\times 10^{-7}$]	R_0	a_0	a_1	χ^2	$D = \epsilon_3 - \epsilon_1$
1.77	6.1	52	0.362	0.00	0.075	38.6
± 0.03	± 0.1	± 1	± 0.007	± 0.00		± 0.6

411
412
413
414
415
416
417
418
419

Figure 4—figure supplement 1. SAXS analysis of liposomes and calculation of bilayer thickness.

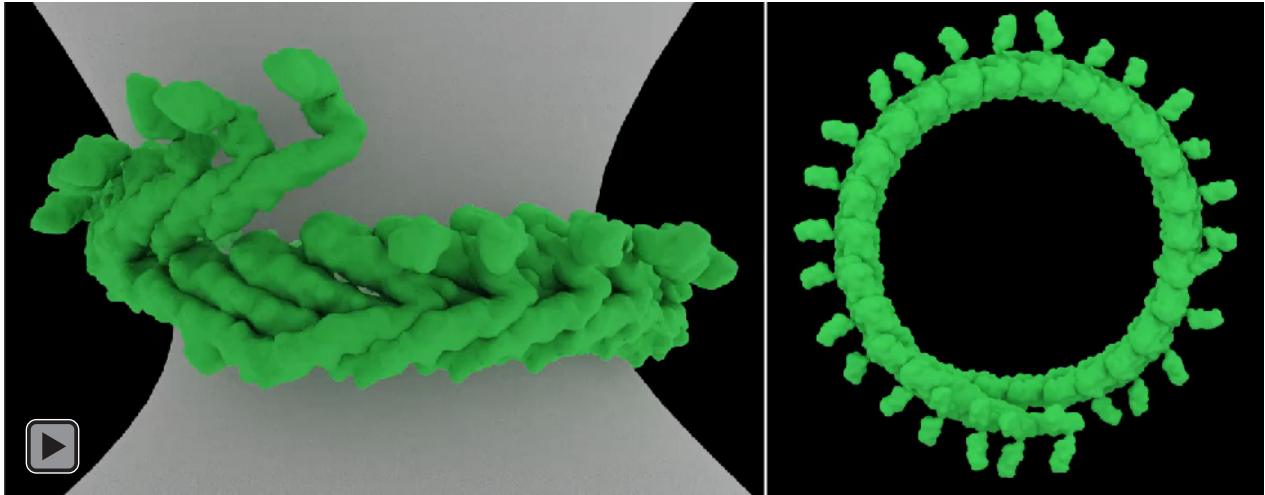
(A) The small angle scattering intensities for protein-free unilamellar vesicles used in this study. The black line represents the fit to the model. The blue data points were used for fitting. (B) Fit results for the liposomes and the resulting thickness, D (Å). The bilayer center, ϵ_2 , was fixed at 0, and the magnitude of the central peak, ρ_2 , was fixed at -1.

420 **Conclusion and Perspective**

421 A remaining central question is how ESCRT-III proteins work with their associated AAA
422 ATPases to catalyze membrane constriction and, ultimately, membrane fission (12, 33, 34, 45-
423 52). Recent in vivo and in vitro studies have explored the roles of staged ESCRT-III assembly
424 (39) and ATP-dependent forces (39, 53). Here, we show how CHMP1B and IST1 function
425 sequentially to squeeze and thin the membrane, bringing it nearly to the fission point (Video 1).
426 Specifically, CHMP1B first binds and assembles into a flexible filament that wraps the target into
427 a moderate curvature tubule. CHMP1B flexibility allows for many degrees of filament curvature
428 and handedness, which may explain how it and other ESCRT-III proteins can adopt a wide range
429 of architectures. IST1 binding then drives CHMP1B to constrict the membrane even further,
430 exploiting IST1-intersubunit interactions to form tighter and tighter turns. Lipid composition is also
431 expected to play a role in this process, although our work does not address that issue directly.

432 Finally, our reconstructions suggest that IST1 may drive CHMP1B into an even narrower
433 constriction state during the fission step, and that this process could be regulated by a VPS4
434 family member. Comparison of the CHMP1B+IST1 and IST1-only filaments suggests that
435 CHMP1B helix $\alpha 6$ (MIM) may sterically limit the full potential of IST1 constriction. We therefore
436 speculate that unfolding or displacement of the CHMP1B MIM could trigger further tightening of
437 the double-stranded filament. Importantly, the CHMP1B MIM forms the binding site for the MIT
438 domains of VPS4 ATPase family members (54-56), and MIT domain binding could therefore
439 provide a mechanism for displacing this helix (34, 35, 39, 48). Further constriction of the
440 CHMP1B+IST1 filament might also push the two aromatic residues of CHMP1B helix $\alpha 1$ (F9 and
441 F13) from the hydrated surface layer, as seen in our structure, into the hydrophobic interior of the
442 outer membrane leaflet, thereby destabilizing the membrane, helping to drive lipid mixing, and
443 promoting fission (57, 58).

444



445

446 **Video 1 – Constriction of a membrane tubule by CHMP1B and IST1.**

447 Table 1. CryoEM data collection parameters

Dataset	CHMP1B-only	CHMP1B+IST1	IST1_{NTD}^{R16E/K27E}
Microscope	Titan Krios	Polara	TF20
Energy filter (slit width, eV)	20	N/A	N/A
Voltage (kV)	300	300	200
C2 aperture (μm)	70	30	70
Objective aperture (μM)	100	100	100
Camera	K2 Summit	K2 Summit	K2 Summit
Detection mode	Super resolution	Super resolution	Super resolution
Pixel size ($\text{\AA}/\text{Pixel}$)	1.345	1.2156	1.234
Total exposure (sec)	10	8.0	8.0
Frame rate (Frames/sec)	0.2	0.2	0.2
Dose rate ($\text{e}^-/\text{\AA}^2/\text{frame}$)	0.90	1.1	1.325
Total dose ($\text{e}^-/\text{\AA}^2$)	45	44	53
Defocus range (μm)	0.23-1.91	0.46-2.97	1.04-3.22
Mean defocus (μm)	1.14	1.54	2.28

448

449

450 Table 2. CryoEM refinement parameters

Dataset	CHMP1B-only	CHMP1B+IST1 (right-handed)	CHMP1B+IST1 (left-handed)	IST1_{NTD}^{R16E/K27E}
Micrographs	3993	9305	9305	279
Segments in final map	9,661	66,149	57,915	4,556
Box size (Å ³)	324	352	352	320
Resolution (Å)	6.2	3.2	3.1	7.2
Helical twist (°)*	+13.86	+20.02	-20.77	+26.85
Helical rise (Å)	1.86	2.96	3.06	3.00
Map sharpening B-factor (Å ²)	-50	-25	-25	-50
Resolution (Å)	6.2	3.2	3.1	7.2

451 *denotes + for right-handed and - for left-handed twists

452

453 Table 3. Model validation statistics

Dataset	CHMP1B- only	CHMP1B+IST1 (right-handed)	CHMP1B+IST1 (left-handed)	IST1 _{NTD} ^{R16E/K27E}
Chains	26	72	68	14
Atoms	32,890	99,216	93,500	19,432
Protein residues	4,238	12,852	12,104	2,534
RMS bonds (Å)	0.006	0.011	0.005	0.007
RMS angles (°)	0.816	0.828	0.863	1.15
MolProbity score	1.55	1.17	1.14	1.61
Clashscore (percentile relative to PDB)	10.73 (68 th)	3.82 (96 th)	7.29 (85 th)	5.48 (93 rd)
Ramachandran favored (%)	98.76	98.58	98.86	95.53
Ramachandran allowed (%)	1.24	1.42	1.14	4.47
Ramachandran outliers (%)	0	0	0	0
Rotamer outliers (%)	0	0	0.34	0.74
C-beta outliers	0	0	0	0
Mean B-factor	N/A*	68	60	N/A*
Minimum/maximum B-factor	N/A*	51/112	45/92	N/A*
EMRinger score	N/A*	1.05	1.41	N/A*

454 *The resolutions of the maps are insufficient to determine these values

455

456 **Materials and Methods**

457 *Protein Expression and Purification*

458 The purification of the N-terminal domain of IST1 containing residues 1-189 (IST1_{NTD}) and
459 the N-terminal IST1 R16E/K27E mutant (IST1_{NTD}^{R16E/K27E}) have been described previously (14).
460 CHMP1B residues 1-199 were cloned into an N-terminal 6xHis-SUMO fusion to yield a native N-
461 terminus after removal of the purification tag. Two alleles of CHMP1B have been reported, 37K
462 or 37E, and we saw that both alleles remodeled membranes and copolymerized with IST1 with
463 indistinguishable activity. The CHMP1B 37E allele was used for subsequent studies and was
464 expressed in LOBSTR-BL21 (DE3) cells (59) in ZYP-5052 auto-induction media (60). Cells were
465 harvested and frozen at -80 °C. All subsequent steps were performed at 4 °C unless otherwise
466 noted. Thawed cells were suspended in lysis buffer (50 mM Tris, pH 8, 500 mM NaCl, 10 mM
467 Imidazole, 1 mM DTT, 5% (v/v) glycerol) and supplemented with lysozyme. Cells were lysed by
468 sonication. Lysate was centrifuged at 30,000 x g for 1 h, and the supernatant was filtered using a
469 0.45 µm membrane. Clarified lysate was loaded onto a gravity flow column with Ni-NTA resin
470 (Qiagen), incubated for 1 hour, and washed extensively with lysis buffer. The fusion protein was
471 eluted in lysis buffer supplemented with 400 mM imidazole. His-tagged ULP1 protease was added
472 and then dialyzed into cleavage buffer (20 mM Tris pH 8.0, 150 mM NaCl, 1 mM DTT, 10 mM
473 imidazole) at room temperature overnight. The cleaved product was then applied again to Ni-
474 NTA resin to remove the purification tag, uncleaved fusion protein, and the protease. CHMP1B
475 was further purified by Superdex-75 16/60 size exclusion chromatography (GE Healthcare Life
476 Sciences, USA) in size exclusion buffer (20 mM Tris, pH 7.4, 150 mM NaCl, 1 mM DTT).

477

478 *Liposome Preparation*

479 Stock lipid solutions (Avanti Polar Lipids) were resuspended in chloroform. To produce the
480 liposomes, (18 mole% 16:0-18:1 phosphatidylserine (POPS), 58% 16:0-22:6 phosphatidylcholine
481 (SDPC), 18% cholesterol, 6% PI(3,5)P₂ or equivalent phosphoinositide), 2 mg total lipid were

482 dried in a glass vial at room temperature under streaming nitrogen with vortexing. The lipids were
483 again re-dissolved in chloroform, dried under streaming nitrogen, and desiccated under house
484 vacuum (at least 4 hours in darkness). The lipid films were dispersed in 1 ml buffer (25 mM Tris,
485 pH 7.4, 150 mM NaCl, 2 mg/ml final concentration, 4 °C overnight with gentle rocking). Liposomes
486 were freeze-thawed 10 times and then stored at -80 °C.

487

488 *Membrane Remodeling Reactions*

489 Membrane remodeling reactions were performed at room temperature with protein
490 concentrations ranging from 5 – 15 μ M and liposome concentrations ranging from 0.5 – 1 mg/ml
491 in reaction buffer (20 mM Tris, pH 7.4, 150 mM NaCl). CHMP1B was incubated with liposomes
492 overnight at room temperature. For membrane-bound CHMP1B reactions, these were then
493 directly used for EM sample preparation. For samples including IST1, the sample was pelleted
494 (13,000 x g, 5 mins), the supernatant was decanted to remove unbound CHMP1B, and the pellet
495 was resuspended in reaction buffer with equimolar IST1_{NTD}. This was incubated for 10 mins and
496 then subjected to EM sample preparation.

497

498 *CryoEM Sample Preparation and Data Collection*

499 3.5 μ L of the membrane remodeling reactions were applied to glow-discharged R1.2/1.3
500 Quantifoil 200 Cu mesh grids (Quantifoil) in a Mark III Vitrobot (FEI). Grids were blotted with
501 Whatman #1 filter paper (Whatman) for 4-8 seconds with a 0 mm offset at 19 °C and 100 %
502 humidity before plunging into liquid ethane. Grids were stored under liquid nitrogen until samples
503 were imaged for structural determination. Datasets were collected either on a 300 kV Technai
504 Polara, a 300 kV Titan Krios, or a 200 kV Technai F20, all using a K2 Summit detector operated
505 in super-resolution mode and binned by a factor of 2 for subsequent processing. Data collection
506 parameters are summarized in Table 1.

507

508 *EM Image Analysis and 3D Reconstructions*

509 All dose-fractionated image stacks were corrected for motion artifacts, 2x binned in the
510 Fourier domain, and dose-weighted using MotionCor2 (61). GCTF-v1.06 (62) was used for
511 contrast transfer function (CTF) estimation. Particles were selected manually using RELION3 with
512 helical processing (63), and subsequent steps were performed in RELION3 unless otherwise
513 stated. Segments were extracted with ~90% overlap between boxes. Multiple rounds of 2D
514 classification were performed to remove poor particles and to yield particles with a largely uniform
515 diameter. For determination of the helical parameters for the CHMP1B-only or IST1_{NTD}^{R16E/K27E}
516 filaments, the iterative helical real space refinement (IHRSR) algorithm (64) as implemented in
517 SPIDER (65) was used. For the CHMP1B+IST1 filaments, the previously determined helical
518 parameters were used as the initial values (14). For all reconstructions, hollow, smooth cylinders
519 were used as initial models for 3D auto-refine reconstructions with refinement of helical
520 parameters and a central Z length of 40% of the particle box and the 'ignore CTFs until first peak'
521 flag for CTF estimation was used. These particles then went through multiple rounds of 3D
522 classification without alignment with 3-4 classes and T values varying from 2-10 and a protein-
523 membrane mask. Selected particles then were subject to another 3D auto-refine reconstruction
524 with per-particle CTF estimation correction within RELION3, followed by a final 3D auto-refine
525 reconstruction. For the membrane-bound left-handed CHMP1B+IST1 reconstruction, initial 3D
526 classification without alignment yielded a class with no discernable features. 2D classification of
527 these particles still yielded class averages with secondary structure features. Refinement of the
528 helical parameters by switching the sign of the twist was then able to generate a good initial 3D
529 reconstruction that was further refined as above. Post-processing was performed using the masks
530 from refinement with ad hoc B-factors applied. Refinement parameters are listed in Table 2.

531

532 *Atomic Modeling and Validation*

533 For the high-resolution CHMP1B+IST1 filaments, a single protomer of CHMP1B and IST1
534 from the previously determined structure were initially docked into the density with UCSF Chimera
535 (66). The protomers were manually adjusted and rebuilt in *Coot* (67) and then refined in
536 phenix.real_space_refine (68) using global minimization, morphing, secondary structure
537 restraints, and local grid search. The refined protomers were then used to generate roughly two
538 full turns manually in real space using UCSF Chimera. Noncrystallographic symmetry (NCS)
539 constraints were then used thorough refinement in phenix.real_space_refine. Iterative cycles of
540 manually rebuilding in *Coot* and phenix.real_space_refine, with previous strategies and
541 additionally B-factor refinement, were performed. For the low resolution CHMP1B-only or IST1_{NTD}
542 filaments, a similar procedure was performed but only roughly one turn was built and no B-factor
543 refinement was performed in phenix.real_space_refine.

544 All final model statistics were tabulated using Molprobity (69) (Table 3). Map versus atomic
545 model FSC plots were computed in PHENIX (70). All structural figures were generated with UCSF
546 Chimera and PyMOL (71).

547

548 *Real-time Imaging of Membrane Constriction*

549 Lipid tube pulling and imaging were performed using a previously described holographic
550 optical trapping setup possessing an independent fluorescent imaging capability (72). Briefly,
551 the setup included a custom-modified Eclipse Ti microscope (Nikon Instruments; Melville, NY),
552 with a Nikon 100X, 1.49NA oil immersion objective, Sapphire 488 excitation laser (Coherent,
553 Santa Clara, CA), and a DU897 camera (Andor Technology, Oxford Instruments, USA). All
554 videos were recorded at 20 fps. Biotinylated giant unilamellar vesicles (GUVs) in Flow Buffer (50
555 mM Tris pH 8.0, 150 mM NaCl, 1 mM DTT,) were synthesized as previously described (73).
556 Biotinylated silica beads (5 μ m diameter, Si5u-BN-1, Nanocs, USA) were incubated with 10 μ M
557 traptavidin (Kerafast, USA) in PMEE buffer (35 mM PIPES, 5 mM MgSO₄, 1 mM EGTA, 0.5 mM
558 EDTA, pH 7.2) for 30 min followed by two rounds of washing (centrifugation at 12,000 \times g for 2

559 minutes followed by supernatant removal and re-suspension of the pellet in 50 mM Tris buffer)
560 to remove excess traptavidin. The beads were then mixed with GUVs and diluted as necessary
561 to limit bead density to 1-3 beads in each 50 μm x 50 μm field of view. The mixture was then
562 applied to a flow cell and immediately subjected to experiments.

563 Membrane tubules were formed by capturing a bead in an optical trap, moving the
564 trapped bead into contact with a GUV, and finally, upon attachment, moving the bead away from
565 the GUV. The presence of a tubule was then assessed visually in real time. The GUVs were
566 stabilized in place via other beads attached to their surface and held in independent
567 holographically defined traps or via non-specific surface attachment. Proteins were introduced
568 into the flow cell in a sequential manner: first 0.5 μM CHMP1B and then 0.5 μM IST1 (both in
569 Flow Buffer). Lipids tubules were held perpendicular to flow direction during these buffer
570 exchanges and the resulting tubule constrictions were recorded. Experiments with CHMP1B
571 and IST1 in slightly different buffers (0.5 μM CHMP1B in 10 mM Tris pH 8.0, 100 mM NaCl 1
572 mM DTT or 0.5 μM IST1 in 50 mM Tris pH7.0, 350 mM NaCl, 5% (v/v) glycerol, 5 mM 2-
573 mercaptoethanol) yielded similar results.

574

575 *Small Angle X-ray Scattering*

576 For small-angle X-ray scattering (SAXS) analysis, liposomes were formed by vortexing a
577 dry lipid film (similar to liposome preparation as stated above) in water to yield a final lipid
578 concentration of 15 mg/ml. Liposomes were extruded through a 100 nm-pore polycarbonate
579 membrane, followed by extrusion through a 50 nm-pore polycarbonate membrane. Synchrotron
580 SAXS data were collected at beamline 4-2 of the Stanford Synchrotron Radiation Lightsource
581 (SSRL), Menlo Park, CA (74). The sample to detector distance was set to 1.1 m, and the X-ray
582 wavelength used was $\lambda = 1.127 \text{ \AA}$ (11 keV). Using a Pilatus 3 X 1M detector (Dectris Ltd,
583 Switzerland) the setup covered a range of momentum transfer of $q \approx 0.017 - 1.17 \text{ \AA}^{-1}$ where q is
584 the magnitude of the scattering vector, defined as $q = 4\pi \sin\theta / \lambda$, where θ is the scattering angle,

585 and λ is the wavelength of the X-rays. Aliquots of 32 μl of freshly extruded vesicles were loaded
586 onto the automated sample loader at the beamline (75). Consecutive series of thirty 2 s exposures
587 were collected first from the buffer blank followed by the vesicle samples. Solutions were
588 oscillated in a stationary quartz capillary cell during data collection to reduce the radiation dose
589 per exposed sample volume. The collected data were radially integrated, analyzed for radiation
590 damage and buffer subtracted using the automated data reduction pipeline at the beam line. To
591 improve statistics and check for reproducibility, the measurements were repeated with different
592 aliquots four times. As no significant differences were found between the repeat measurements,
593 the different data sets were averaged together.

594 The buffer-subtracted and averaged data were fit using a model for unilamellar vesicles
595 (76) as previously described (77). The electron density profile of the bilayer is approximated by
596 three Gaussian peaks corresponding to the inner and outer phosphate peaks and a negative peak
597 at the center for the hydrocarbon region. The following Equation 1 was used to fit the data:

598

$$599 \quad I(q) = I_0 q^{-2} \sum_{i,j}^{n=3} (R_0 + \epsilon_i)(R_0 + \epsilon_j) \rho_i \rho_j \sigma_i \sigma_j \exp[-q^2(\sigma_i^2 + \sigma_j^2)/2] \cos[q(\epsilon_i - \epsilon_j)] + a_0 + a_1 q \quad (1)$$

600

601 where R_0 is the mean radius of the vesicle measured from the center of the bilayer, ϵ is the peak
602 displacement from the bilayer center, σ the Gaussian width of the peak and ρ is its amplitude. I_0
603 is the overall intensity of the measured profile. A background term was added, consisting of a
604 constant a_0 and a linear term a_1 , to take into account the contribution from possible lateral
605 correlations between the lipids. The measured data were fit in the q -region between $q = 0.02 -$
606 0.6 \AA^{-1} (depicted as blue colored points in Figure 4—figure supplement 1A). First, the data were
607 fit using a simulated annealing routine, and the results were then further optimized using a non-
608 linear least square algorithm, both by using code from the open source GNU scientific
609 library project (<https://www.gnu.org/software/gsl/>). The final fit parameters including the final χ^2

610 value of the fits and the resulting bilayer thickness (measured as distance between the inner and
611 outer leaflet peak positions) are summarized in Figure 4—figure supplement 1B.

612

613 *Image Analysis of Membrane Bilayer*

614 To determine the bilayer thickness and relative intensity of inner and outer leaflets, Fiji
615 (78, 79) was used. The cryoEM half maps from the C1 reconstructions were each low-pass filtered
616 to 8 Å, summed along the central 40% along the Z-axis, and the maps were radially averaged
617 using the Radial Profile Extended plugin (80) to determine the intensities as a function of radius,
618 resulting in two measurements per reconstruction. 2D averages of liposomes (n=6) were low pass
619 filtered to 20 Å, parameters for a circle that defined the 2D average were determined, and a wedge
620 that best covered the image was then used to calculate the intensities. For all resulting plots, the
621 radial intensities were normalized to the peak intensity of the inner leaflet peak and then fit to a
622 three Gaussian model (81) similar to the SAXS measurements. The model was minimized by a
623 non-linear least square algorithm and the fit errors between the data and models ranged from
624 1.45%-3.30% with R² values from 0.996-0.999. The local maxima for the headgroups were used
625 to determine the bilayer thickness and inner/outer leaflet intensity ratios.

626

627 **Accession Numbers**

628 CryoEM maps and models were deposited to the PDB and EMDB with the following codes:
629 membrane-bound CHMP1B-only filament (PDB ID: 6TZ9, EMD-20590), membrane-bound right
630 handed CHMP1B+IST1 filament (PDB ID: 6TZ4, EMD-20588), membrane-bound left handed
631 CHMP1B+IST1 filament (PDB ID: 6TZ5, EMD-20589), IST1_{NTD}^{R16E/K27E} filament (PDB ID: 6TZA,
632 EMD-20591).

633

634 **Acknowledgements**

635 We thank members of the Frost lab for helpful discussion, and especially Paul Thomas
636 with computational assistance. We thank Michael Grabe, Maxwell Tucker, David Argudo, Ed
637 Lyman, Alex Sodt, Greg Huber, and Aurelien Roux for discussions on membrane biophysical
638 behavior. We thank Thomas Weiss for assistance with SAXS data collection. We thank Michael
639 Braunfeld, David Bulkley, Matt Harrington, Alexander Myasnikov, and Zanlin Yu of the UCSF
640 Center for Advanced CryoEM for microscopy support. We thank Joshua Baker-LePain and the
641 QB3 shared cluster (NIH grant 1S10OD021596-01) for computational support. Structural biology
642 applications used in this project were compiled and configured by SBGrid (82). The Titan X Pascal
643 used for this research was donated by the NVIDIA Corporation. This work was supported by NIH
644 grants P50 082545 and 1DP2GM110772-01 (to A.F.), R01 GM112080 and R37 AI51174 (to
645 W.I.S.), A.F. is further supported by a Faculty Scholar grant from the HHMI and is a Chan
646 Zuckerberg Biohub investigator.

647

648 **Competing Interests**

649 The authors declare no competing interests.

650

651 **References**

- 652 1. J. H. Hurley, ESCRTs are everywhere. *EMBO J* **34**, 2398-2407 (2015).
- 653 2. J. McCullough, L. A. Colf, W. I. Sundquist, Membrane fission reactions of the mammalian
654 ESCRT pathway. *Annu Rev Biochem* **82**, 663-692 (2013).
- 655 3. W. I. Sundquist, H. G. Krausslich, HIV-1 assembly, budding, and maturation. *Cold Spring*
656 *Harb Perspect Med* **2**, a006924 (2012).
- 657 4. Y. Olmos, L. Hodgson, J. Mantell, P. Verkade, J. G. Carlton, ESCRT-III controls nuclear
658 envelope reformation. *Nature* **522**, 236-239 (2015).
- 659 5. M. Vietri *et al.*, Spastin and ESCRT-III coordinate mitotic spindle disassembly and nuclear
660 envelope sealing. *Nature* **522**, 231-235 (2015).
- 661 6. M. Raab *et al.*, ESCRT III repairs nuclear envelope ruptures during cell migration to limit
662 DNA damage and cell death. *Science* **352**, 359-362 (2016).
- 663 7. C. M. Denais *et al.*, Nuclear envelope rupture and repair during cancer cell migration.
664 *Science* **352**, 353-358 (2016).
- 665 8. Y. Olmos, A. Perdrix-Rosell, J. G. Carlton, Membrane Binding by CHMP7 Coordinates
666 ESCRT-III-Dependent Nuclear Envelope Reformation. *Curr Biol*, (2016).
- 667 9. M. L. Skowyra, P. H. Schlesinger, T. V. Naismith, P. I. Hanson, Triggered recruitment of
668 ESCRT machinery promotes endolysosomal repair. *Science* **360**, (2018).

- 669 10. C. L. Chang *et al.*, Spastin tethers lipid droplets to peroxisomes and directs fatty acid
670 trafficking through ESCRT-III. *J Cell Biol*, (2019).
- 671 11. F. D. Mast *et al.*, ESCRT-III is required for scissioning new peroxisomes from the
672 endoplasmic reticulum. *J Cell Biol* **217**, 2087-2102 (2018).
- 673 12. J. McCullough, A. Frost, W. I. Sundquist, Structures, Functions, and Dynamics of ESCRT-
674 III/Vps4 Membrane Remodeling and Fission Complexes. *Annu Rev Cell Dev Biol* **34**, 85-
675 109 (2018).
- 676 13. R. Allison *et al.*, Defects in ER-endosome contacts impact lysosome function in hereditary
677 spastic paraplegia. *J Cell Biol* **216**, 1337-1355 (2017).
- 678 14. J. McCullough *et al.*, Structure and membrane remodeling activity of ESCRT-III helical
679 polymers. *Science* **350**, 1548-1551 (2015).
- 680 15. R. Allison *et al.*, An ESCRT-spastin interaction promotes fission of recycling tubules from
681 the endosome. *J Cell Biol* **202**, 527-543 (2013).
- 682 16. M. Bajorek *et al.*, Structural basis for ESCRT-III protein autoinhibition. *Nat Struct Mol Biol*
683 **16**, 754-762 (2009).
- 684 17. T. Muziol *et al.*, Structural basis for budding by the ESCRT-III factor CHMP3. *Dev Cell* **10**,
685 821-830 (2006).
- 686 18. J. Xiao *et al.*, Structural basis of Ist1 function and Ist1-Did2 interaction in the multivesicular
687 body pathway and cytokinesis. *Mol Biol Cell* **20**, 3514-3524 (2009).
- 688 19. P. I. Hanson, R. Roth, Y. Lin, J. E. Heuser, Plasma membrane deformation by circular
689 arrays of ESCRT-III protein filaments. *J Cell Biol* **180**, 389-402 (2008).
- 690 20. S. Lata *et al.*, Structural basis for autoinhibition of ESCRT-III CHMP3. *J Mol Biol* **378**, 818-
691 827 (2008).
- 692 21. Y. Lin, L. A. Kimpler, T. V. Naismith, J. M. Lauer, P. I. Hanson, Interaction of the
693 mammalian endosomal sorting complex required for transport (ESCRT) III protein hSnf7-
694 1 with itself, membranes, and the AAA+ ATPase SKD1. *J Biol Chem* **280**, 12799-12809
695 (2005).
- 696 22. S. Tang *et al.*, Structural basis for activation, assembly and membrane binding of ESCRT-
697 III Snf7 filaments. *Elife* **4**, (2015).
- 698 23. B. J. McMillan *et al.*, Electrostatic Interactions between Elongated Monomers Drive
699 Filamentation of *Drosophila* Shrub, a Metazoan ESCRT-III Protein. *Cell Rep* **16**, 1211-
700 1217 (2016).
- 701 24. I. H. Lee, H. Kai, L. A. Carlson, J. T. Groves, J. H. Hurley, Negative membrane curvature
702 catalyzes nucleation of endosomal sorting complex required for transport (ESCRT)-III
703 assembly. *Proc Natl Acad Sci U S A* **112**, 15892-15897 (2015).
- 704 25. X. Crespo-Yanez *et al.*, CHMP1B is a target of USP8/UBPY regulated by ubiquitin during
705 endocytosis. *PLoS Genet* **14**, e1007456 (2018).
- 706 26. W. Stoorvogel, V. Oorschot, H. J. Geuze, A novel class of clathrin-coated vesicles budding
707 from endosomes. *J Cell Biol* **132**, 21-33 (1996).
- 708 27. M. M. Manni *et al.*, Acyl chain asymmetry and polyunsaturation of brain phospholipids
709 facilitate membrane vesiculation without leakage. *Elife* **7**, (2018).
- 710 28. M. Pinot *et al.*, Lipid cell biology. Polyunsaturated phospholipids facilitate membrane
711 deformation and fission by endocytic proteins. *Science* **345**, 693-697 (2014).
- 712 29. N. Talledge *et al.*, The ESCRT-III proteins IST1 and CHMP1B assemble around nucleic
713 acids. *bioRxiv*, (2018).
- 714 30. A. G. Cashikar *et al.*, Structure of cellular ESCRT-III spirals and their relationship to HIV
715 budding. *Elife* **3**, (2014).
- 716 31. H. C. Hyman, S. Trachtenberg, Point mutations that lock *Salmonella typhimurium* flagellar
717 filaments in the straight right-handed and left-handed forms and their relation to filament
718 superhelicity. *J Mol Biol* **220**, 79-88 (1991).

- 719 32. S. Maki-Yonekura, K. Yonekura, K. Namba, Conformational change of flagellin for
720 polymorphic supercoiling of the flagellar filament. *Nat Struct Mol Biol* **17**, 417-422 (2010).
- 721 33. J. Schoneberg, I. H. Lee, J. H. Iwasa, J. H. Hurley, Reverse-topology membrane scission
722 by the ESCRT proteins. *Nat Rev Mol Cell Biol*, (2016).
- 723 34. N. Chiaruttini *et al.*, Relaxation of Loaded ESCRT-III Spiral Springs Drives Membrane
724 Deformation. *Cell* **163**, 866-879 (2015).
- 725 35. B. E. Mierzwa *et al.*, Dynamic subunit turnover in ESCRT-III assemblies is regulated by
726 Vps4 to mediate membrane remodelling during cytokinesis. *Nat Cell Biol* **19**, 787-798
727 (2017).
- 728 36. I. Goliand *et al.*, Resolving ESCRT-III Spirals at the Intercellular Bridge of Dividing Cells
729 Using 3D STORM. *Cell Rep* **24**, 1756-1764 (2018).
- 730 37. J. Guizetti *et al.*, Cortical constriction during abscission involves helices of ESCRT-III-
731 dependent filaments. *Science* **331**, 1616-1620 (2011).
- 732 38. S. Banjade, S. Tang, Y. H. Shah, S. D. Emr, Electrostatic lateral interactions drive ESCRT-
733 III heteropolymer assembly. *Elife* **8**, (2019).
- 734 39. A.-K. Pfitzner, V. Mercier, A. Roux, Vps4 triggers sequential subunit exchange in ESCRT-
735 III polymers that drives membrane constriction and fission. *bioRxiv*, (2019).
- 736 40. K. Rajamoorthi, H. I. Petrache, T. J. McIntosh, M. F. Brown, Packing and viscoelasticity of
737 polyunsaturated omega-3 and omega-6 lipid bilayers as seen by (2)H NMR and X-ray
738 diffraction. *J Am Chem Soc* **127**, 1576-1588 (2005).
- 739 41. R. Lipowsky, Coupling of bending and stretching deformations in vesicle membranes. *Adv*
740 *Colloid Interface Sci* **208**, 14-24 (2014).
- 741 42. B. Rozycki, R. Lipowsky, Spontaneous curvature of bilayer membranes from molecular
742 simulations: asymmetric lipid densities and asymmetric adsorption. *J Chem Phys* **142**,
743 054101 (2015).
- 744 43. J. M. Allain, C. Storm, A. Roux, M. Ben Amar, J. F. Joanny, Fission of a multiphase
745 membrane tube. *Phys Rev Lett* **93**, 158104 (2004).
- 746 44. J. Liu, M. Kaksonen, D. G. Drubin, G. Oster, Endocytic vesicle scission by lipid phase
747 boundary forces. *Proc Natl Acad Sci U S A* **103**, 10277-10282 (2006).
- 748 45. N. Chiaruttini, A. Roux, Dynamic and elastic shape transitions in curved ESCRT-III
749 filaments. *Curr Opin Cell Biol* **47**, 126-135 (2017).
- 750 46. M. Lenz, S. Morlot, A. Roux, Mechanical requirements for membrane fission: common
751 facts from various examples. *FEBS Lett* **583**, 3839-3846 (2009).
- 752 47. G. Fabrikant *et al.*, Computational model of membrane fission catalyzed by ESCRT-III.
753 *PLoS Comput Biol* **5**, e1000575 (2009).
- 754 48. S. Maity *et al.*, VPS4 triggers constriction and cleavage of ESCRT-III helical filaments. *Sci*
755 *Adv* **5**, eaau7198 (2019).
- 756 49. W. M. Henne, N. J. Buchkovich, S. D. Emr, The ESCRT pathway. *Dev Cell* **21**, 77-91
757 (2011).
- 758 50. S. Peel, P. Macheboeuf, N. Martinelli, W. Weissenhorn, Divergent pathways lead to
759 ESCRT-III-catalyzed membrane fission. *Trends Biochem Sci* **36**, 199-210 (2011).
- 760 51. L. Harker-Kirschneck, B. Baum, A. Saric, Transitions in filament geometry drive ESCRT-
761 III-mediated membrane remodelling and fission. *bioRxiv*, (2019).
- 762 52. J. M. von Filseck *et al.*, Anisotropic ESCRT-III architecture governs helical membrane tube
763 formation. *bioRxiv*, (2019).
- 764 53. J. Schoneberg *et al.*, ATP-dependent force generation and membrane scission by
765 ESCRT-III and Vps4. *Science* **362**, 1423-1428 (2018).
- 766 54. R. Y. Samson, T. Obita, S. M. Freund, R. L. Williams, S. D. Bell, A role for the ESCRT
767 system in cell division in archaea. *Science* **322**, 1710-1713 (2008).
- 768 55. M. D. Stuchell-Breton *et al.*, ESCRT-III recognition by VPS4 ATPases. *Nature* **449**, 740-
769 744 (2007).

- 770 56. D. Yang *et al.*, Structural basis for midbody targeting of spastin by the ESCRT-III protein
771 CHMP1B. *Nat Struct Mol Biol* **15**, 1278-1286 (2008).
- 772 57. L. V. Chernomordik, M. M. Kozlov, Mechanics of membrane fusion. *Nat Struct Mol Biol*
773 **15**, 675-683 (2008).
- 774 58. A. L. Lai, H. Park, J. M. White, L. K. Tamm, Fusion peptide of influenza hemagglutinin
775 requires a fixed angle boomerang structure for activity. *J Biol Chem* **281**, 5760-5770
776 (2006).
- 777 59. K. R. Andersen, N. C. Leksa, T. U. Schwartz, Optimized E. coli expression strain LOBSTR
778 eliminates common contaminants from His-tag purification. *Proteins* **81**, 1857-1861
779 (2013).
- 780 60. F. W. Studier, Protein production by auto-induction in high density shaking cultures.
781 *Protein expression and purification* **41**, 207-234 (2005).
- 782 61. S. Q. Zheng *et al.*, MotionCor2: anisotropic correction of beam-induced motion for
783 improved cryo-electron microscopy. *Nat Methods* **14**, 331-332 (2017).
- 784 62. K. Zhang, Gctf: Real-time CTF determination and correction. *J Struct Biol* **193**, 1-12
785 (2016).
- 786 63. S. He, S. H. W. Scheres, Helical reconstruction in RELION. *J Struct Biol* **198**, 163-176
787 (2017).
- 788 64. E. H. Egelman, A robust algorithm for the reconstruction of helical filaments using single-
789 particle methods. *Ultramicroscopy* **85**, 225-234 (2000).
- 790 65. J. Frank *et al.*, SPIDER and WEB: processing and visualization of images in 3D electron
791 microscopy and related fields. *J Struct Biol* **116**, 190-199 (1996).
- 792 66. E. F. Pettersen *et al.*, UCSF Chimera--a visualization system for exploratory research and
793 analysis. *J Comput Chem* **25**, 1605-1612 (2004).
- 794 67. P. Emsley, B. Lohkamp, W. G. Scott, K. Cowtan, Features and development of Coot. *Acta*
795 *Crystallogr D Biol Crystallogr* **66**, 486-501 (2010).
- 796 68. P. V. Afonine *et al.*, Real-space refinement in PHENIX for cryo-EM and crystallography.
797 *Acta Crystallogr D Struct Biol* **74**, 531-544 (2018).
- 798 69. C. J. Williams *et al.*, MolProbity: More and better reference data for improved all-atom
799 structure validation. *Protein Sci* **27**, 293-315 (2018).
- 800 70. P. V. Afonine *et al.*, New tools for the analysis and validation of cryo-EM maps and atomic
801 models. *Acta Crystallogr D Struct Biol* **74**, 814-840 (2018).
- 802 71. Schrodinger, LLC. (2015).
- 803 72. J. Bergman, O. Osunbayo, M. Vershinin, Constructing 3D microtubule networks using
804 holographic optical trapping. *Sci Rep* **5**, 18085 (2015).
- 805 73. V. Romanov, J. McCullough, B. K. Gale, A. Frost, A Tunable Microfluidic Device Enables
806 Cargo Encapsulation by Cell- or Organelle-Sized Lipid Vesicles Comprising Asymmetric
807 Lipid Bilayers. *Advanced Biosystems* **3**, 1900010 (2019).
- 808 74. I. L. Smolsky *et al.*, Biological small-angle x-ray scattering facility at the Stanford
809 synchrotron radiation laboratory. *J Appl Crystallogr* **40**, S453-S458 (2007).
- 810 75. A. Martel, P. Liu, T. M. Weiss, M. Niebuhr, H. Tsuruta, An integrated high-throughput data
811 acquisition system for biological solution X-ray scattering studies. *J Synchrotron Radiat*
812 **19**, 431-434 (2012).
- 813 76. M. R. Brzustowicz, A. T. Brunger, X-ray scattering from unilamellar lipid vesicles. *J Appl*
814 *Crystallogr* **38**, 126-131 (2005).
- 815 77. F. R. Moss, 3rd *et al.*, Ladderane phospholipids form a densely packed membrane with
816 normal hydrazine and anomalously low proton/hydroxide permeability. *Proc Natl Acad Sci*
817 *U S A* **115**, 9098-9103 (2018).
- 818 78. J. Schindelin *et al.*, Fiji: an open-source platform for biological-image analysis. *Nat*
819 *Methods* **9**, 676-682 (2012).

- 820 79. C. T. Rueden *et al.*, ImageJ2: ImageJ for the next generation of scientific image data. *BMC*
821 *Bioinformatics* **18**, 529 (2017).
- 822 80. P. Carl, Radial Profile Extended. [http://questpharma.u-strasbg.fr/html/radial-profile-](http://questpharma.u-strasbg.fr/html/radial-profile-ext.html)
823 [ext.html](http://questpharma.u-strasbg.fr/html/radial-profile-ext.html). (2017).
- 824 81. T. O'Haver, Curve fitting C: Non-linear Iterative Curve Fitting.
825 <https://terpconnect.umd.edu/%7Etoh/spectrum/CurveFittingC.html>. (2019).
- 826 82. A. Morin *et al.*, Collaboration gets the most out of software. *Elife* **2**, e01456 (2013).
827